

AD/A-001 003

STRESS WAVE CHARACTERIZATION OF AVCO  
3D CARBON-CARBON (3DDC). VOLUME 1

Bobby L. Bracewell, et al

Kaman Sciences Corporation

Prepared for:

Defense Nuclear Agency

20 May 1974

DISTRIBUTED BY:

**NTIS**

National Technical Information Service  
U. S. DEPARTMENT OF COMMERCE

UNCLASSIFIED

SECURITY CLASSIFICATION OF THIS PAGE (When Data Entered)

AD/A-001003

REPORT DOCUMENTATION PAGE		READ INSTRUCTIONS BEFORE COMPLETING FORM
1. REPORT NUMBER DNA 3424F-1	2. GOVT ACCESSION NO.	3. RECIPIENT'S CATALOG NUMBER
4. TITLE (and Subtitle) Stress Wave Characterization of AVCO 3D Carbon-Carbon (3DCC) - Volume 1		5. TYPE OF REPORT & PERIOD COVERED Final Report
		6. PERFORMING ORG. REPORT NUMBER
7. AUTHOR(s) Bobby L. Bracewell Thomas F. V. Meagher James C. Nickell		8. CONTRACT OR GRANT NUMBER(s) DNA001-72-C-0202
9. PERFORMING ORGANIZATION NAME AND ADDRESS Kaman Sciences Corporation 1500 Garden of the Gods Road Colorado Springs, Colorado 80907		10. PROGRAM ELEMENT, PROJECT, TASK AREA & WORK UNIT NUMBERS NWED N99QAXAC310-04
11. CONTROLLING OFFICE NAME AND ADDRESS Director Defense Nuclear Agency Washington, D. C. 20305		12. REPORT DATE May 20, 1974
		13. NUMBER OF PAGES 83
14. MONITORING AGENCY NAME & ADDRESS (if different from Controlling Office)		15. SECURITY CLASS (of this report) UNCLASSIFIED
		15a. DECLASSIFICATION DOWNGRADING SCHEDULE
16. DISTRIBUTION STATEMENT (of this Report)  "Approved for public release; distribution unlimited".		
17. DISTRIBUTION STATEMENT (of the abstract entered in Block 20, if different from Report)  Reproduced by NATIONAL TECHNICAL INFORMATION SERVICE U. S. Department of Commerce Springfield, VA 22151		
18. SUPPLEMENTARY NOTES  "This work was sponsored by the Defense Nuclear Agency under Subtask N99QAXAC310-04."		
19. KEY WORDS (Continue on reverse side if necessary and identify by block number) Shock Wave Testing                      Hydrocode Correlation Gas Gun Testing Hugoniot Testing Equation-of-State Testing Carbon-Carbon Material		
20. ABSTRACT (Continue on reverse side if necessary and identify by block number) The shock wave characteristics of an AVCO three-dimensional weave, carbon-carbon material (AVCO 3DCC) were experimentally investigated and analytically modeled. Using the Kaman Sciences Corporation gas gun facility, Hugoniot and wave attenuation tests were performed on flat specimens cut from arcs of the material. From these tests, equation-of-state inputs for use with the PUFF computer code were derived and utilized to make correlations with the wave attenuation experiments. Explanation of the 3DCC material		

UNCLASSIFIED

SECURITY CLASSIFICATION OF THIS PAGE (When Data Entered)

behavior is given based upon the degree of correlation between the calculations and experiments.

11

UNCLASSIFIED

SECURITY CLASSIFICATION OF THIS PAGE (When Data Entered)

## SUMMARY

The work reported here was undertaken to experimentally and analytically characterize an AVCO three-dimensional weave carbon-carbon material (AVCO 3DCC) in order to facilitate assessment of its performance in nuclear weapons environments. This was accomplished in two steps. First, the KSC gas gun facility was used to perform Hugoniot and wave attenuation experiments suitable to provide equation-of-state data on the material. Second, the data was used to derive inputs for the PUFF hydrocode, which was then utilized to make calculations simulating some of the wave attenuation experiments. The correlation between the PUFF code calculations and the experiments enabled assessment of the accuracy of the model derived.

The  $P-\mu$  equation-of-state (for use with the PUFF code) derived from the Hugoniot testing was determined to be

$$P(\mu) = 0.028\mu - 0.2239\mu^2 + 1.409\mu^3$$

with  $\rho_0 = 1.65 \text{ gm/cm}^3$ . This equation is compatible with the normal cubic form of equation-of-state found in the PUFF code. A better match with the data was obtained by using the rational polynomial fit

$$P(\mu) = \frac{0.006302\mu + 0.006485\mu^2 + 0.1488\mu^3}{0.4251 + 0.2034\mu - 2.555\mu^2}$$

which is not good for  $\mu$  near 0.45 and requires modification of the PUFF code for use.

The wave attenuation experiments indicated widely different wave velocities through the radial and lateral parts of the material. In the geometry tested (with the

waves propagating down the radials) the area averaged pressure profile was quite similar to that of a planar shock wave with a precursor. Due to this similarity, a standard  $P-\alpha$  dynamic compaction model was used to make computer correlations with some of the wave attenuation experiments. The  $P-\alpha$  model was able to predict the stress wave response of the material on an area averaging basis. However, the model assumes planar motion in both the precursor and main shock waves, whereas the probable material behavior has a highly non-planar initial wave with fast motion down the radials and only slight coupling with the surrounding material.

## PREFACE

These material characterization efforts were accomplished as a part of the DNA sponsored Carbon-Carbon Design Program (CCDP) under the direction of Captain T. Swartz. The work authorization was covered by DNA contract No. DNA-001-72-C-0202. Additional direction was obtained from Capt. J. Green, Space and Missile Systems Organization (SAMSO); Capt. F. Bick, Air Force Weapons Laboratory (AFWL); and Mr. W. E. Schorr, Aerospace Corporation.

## TABLE OF CONTENTS

<u>SECTION</u>		<u>PAGE</u>
I	INTRODUCTION	9
II	HUGONIOT TESTING	11
	1. Sample Preparation and Test Procedure	11
	2. Derivation of PUFF Code Inputs	14
III	WAVE ATTENUATION TESTING	26
	1. Sample Preparation and Test Procedure	26
	2. Computer Code Correlation	34
 <u>APPENDIX</u>		
A	THEORETICAL BACKGROUND	43
	1. Theoretical Description of Shock Behavior	43
	2. Basic Thermodynamics of Shock Waves	47
	3. Computer Methods	53
	4. Derivation of Computer Code Inputs	55
B	EXPERIMENTAL TECHNIQUE	61
	1. Gas Gun Facility	61
	2. Set-Up and Alignment Procedures	65
	3. Piezoelectric Quartz Gage	69
	4. Piezoresistive Manganin Gage	78
	5. Curved Sample Testing	80
	6. Additional Gas Gun Techniques	81

## LIST OF ILLUSTRATIONS

<u>FIGURE</u>		<u>PAGE</u>
1	Test Configuration for 3DCC Hugoniot Tests	12
2	Interpretation of a Test Using Tungsten Carbide Buffer	13
3	Experimental Records from Tests 1017 and 1034	15
4	Experimental Records from Tests 1035 and 1036	16
5	Experimental Records from Tests 1052 and 1053	17
6	Experimental Record from Test 1054	18
7	Peak Pressure-Particle Velocity Point for Test 1036	20
8	Best Fit Hugoniot Curve for 3DCC	21
9	P- $\mu$ Hugoniot for 3DCC	23
10	Rational Polynomial P- $\mu$ Fit for 3DCC Hugoniot	25
11	Test Configuration for 3DCC Transmitted Wave Tests	28
12	Experimental Record from Test 1095	31
13	3DCC Wave Profile Measurements	32
14	3DCC Wave Profile Measurements	33
15	AVCO 3DCC Equation of State	35
16	Wave Profile Comparison Tests 1089 and 1090	37
17	Wave Profile Comparison Test 1096	38
18	Wave Profile Comparison Test 1098	39
A-1	Comparison of Various Curves in the (P-V) Plane	48
B-1	Schematic Diagram of KSC Gas Gun Facility	62
B-2	Typical Gas Gun Projectile	63
B-3	Target Alignment	67
B-4	Action of Quartz Transducer	70
B-5	Quartz Crystal with Shorted Guard Ring	72
B-6	Typical Quartz-Target Assembly	72



LIST OF ILLUSTRATIONS (Continued)

<u>FIGURE</u>		<u>PAGE</u>
B-7	Calibration Curve for 1" x 1/4" Quartz Crystal	73
B-8	Action of Buffer Disc on Shock Front	76

## TABLES

<u>NUMBER</u>		<u>PAGE</u>
1	Summary of 3DCC Hugoniot Tests	19
2	3DCC Stress Wave Attenuation Tests Summary Table	30

## SECTION I

### INTRODUCTION

The shock wave characteristics of a three-dimensional weave, carbon-carbon material have been experimentally investigated and analytically modeled. This AVCO fabricated material consists of WYB graphite radials and Thornel 50 tape laterals formed together in a graphitized matrix. The matrix material is formed by impregnating the woven structure with SC1008 resin and the entire matrix is then pyrolyzed and graphitized. The material is commonly referred to as AVCO 3DCC.

The studies for this material were conducted with the shock waves propagating in the directions of the radials; thus shock waves propagate down the radials and through the lateral layers at the same time. As a result of the different shock propagation characteristics of these two regions, an aplanar shock wave is created wherein the disturbance in the radial tends to lead that through the laterals. On an area averaging basis, these waves combine in a manner which appears to be similar to the two wave structure created in a material with a yield point; i.e., the area averaged 3DCC shock wave structure is undistinguishable from a planar shock wave which has a precursor. Due to this similarity, a standard P- $\alpha$  planar wave model was used to model the 3DCC material; hence, at the expense of using a somewhat erroneous model, conventional hydrocodes can be used to conduct design studies and predict experimental results.

The tests are described in detail in Section II and III and a full description of shock testing, the KSC gas gun facility, and experimental techniques is given in Appendices A and B.

## SECTION II

### HUGONIOT TESTING

#### 1. Sample Preparation and Test Procedure

Due to the cylindrical geometry used in fabricating the 3DCC material, samples were received in the form of arc segments cut from cylindrical rings. KSC has developed the technique of performing transmitted wave tests on such arc segments using its gas gun facility. However, since techniques for performing Hugoniot tests on curved samples had not been developed, it was necessary to use the usual flat geometry for the testing reported here.

Disc shaped samples were cut from the arc segments and mounted on projectiles, as shown schematically in Figure 1. Samples were mounted so that impact occurred on the "outside" surface of the cylinder from which the arcs were cut. Tungsten carbide (WC) buffers were used over quartz crystal transducers for these tests, in order to eliminate uneven loading of the quartz front face (see Appendix B). This arrangement is also shown schematically in Figure 1. Results of a test using this configuration are interpreted using the known behavior of quartz and tungsten carbide, as shown in Figure 2. The initial impact of the samples on the WC buffer at velocity  $u_p$  induces in both materials the pressure-particle velocity state indicated by point A. After the shock wave propagates through the WC buffer, it is partially relieved to state B upon passage into the quartz due to the impedance mismatch at the WC-quartz interface. The pressure history experienced by the quartz (represented by point B) is recorded during a test. This information is converted to

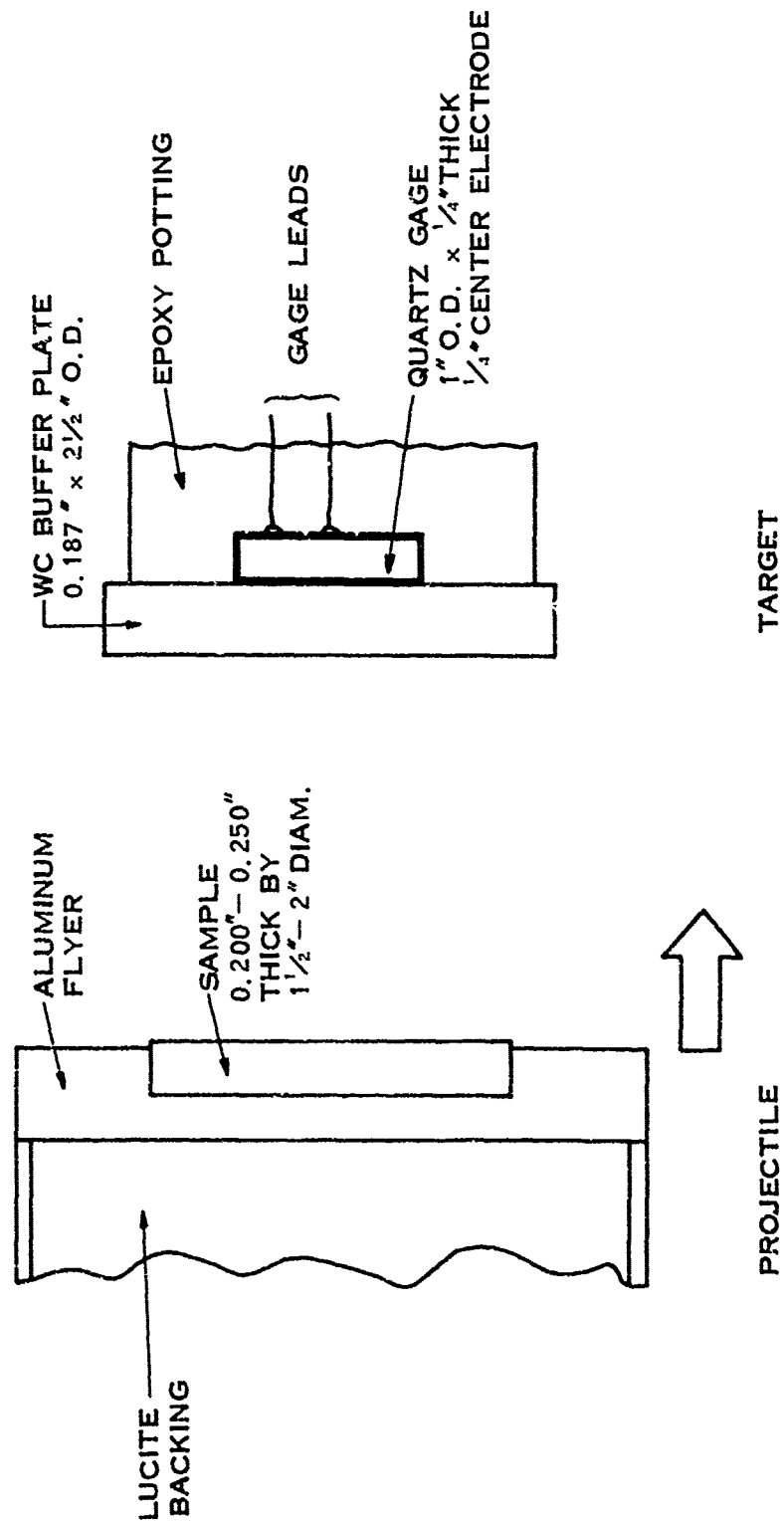


FIGURE 1 TEST CONFIGURATION FOR 3DCC HUGONIOT TESTS

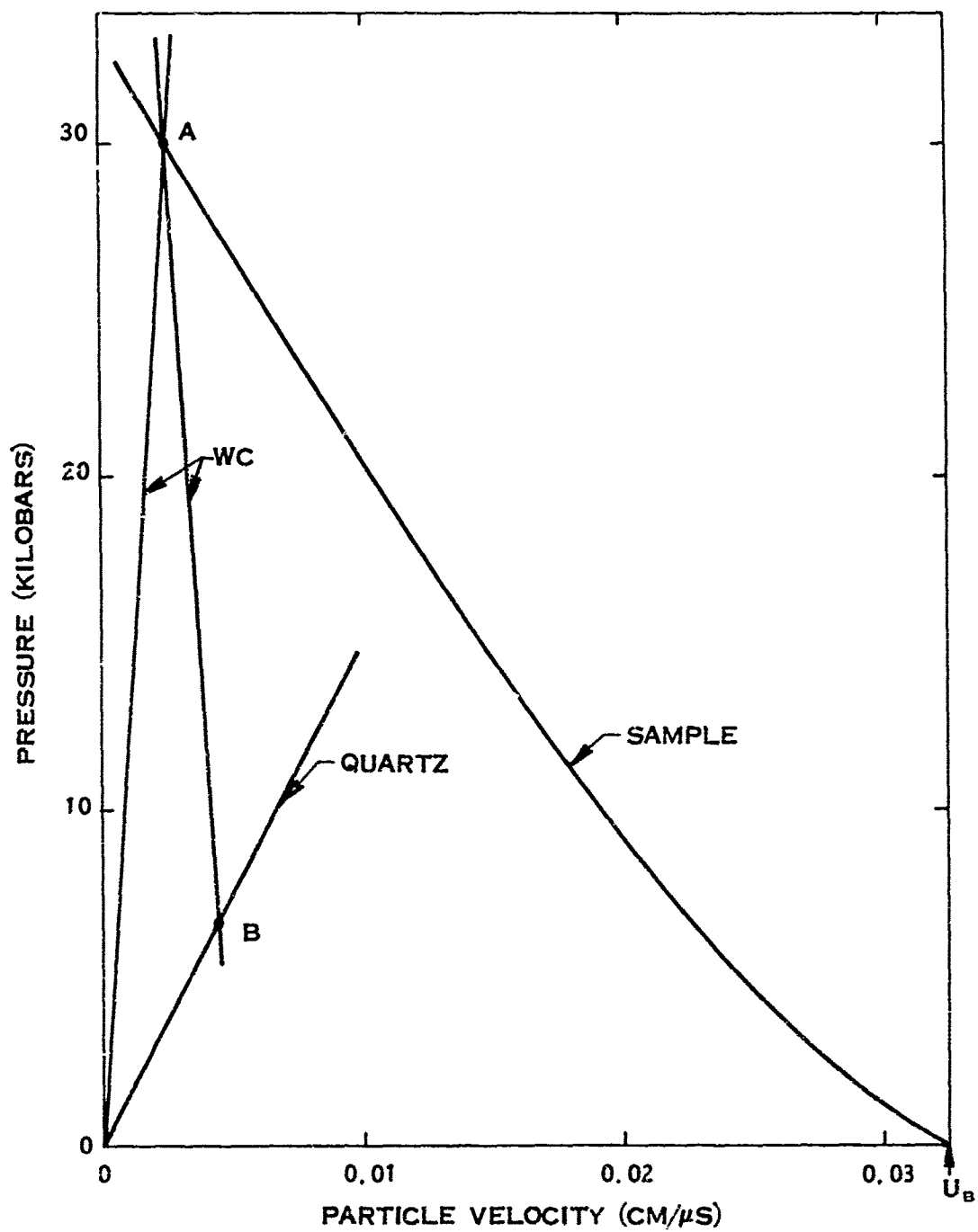


FIGURE 2 INTERPRETATION OF A TEST USING TUNGSTEN CARBIDE BUFFER

the pressure history experienced by the WC buffer and the sample (represented by point A) using the known behavior of quartz and tungsten carbide.

Utilizing various impact velocities, eight tests were performed to cover the pressure range from about 2 to 30 kb. Oscilloscope records from these tests are shown in Figures 3 through 6. Table 1 provides a summary of the results from these tests. Examination of the records shows evidence of the structure of the materials. In all cases, the peak pressure-particle velocity state listed in Table 1 was taken to be the initial peak reached before any relief or ramping occurred. For example, the point chosen in test 1036 is indicated in Figure 7. Note that the pressure scale in Figure 7 applies to the quartz gage, not to the sample. The sample Hugoniot pressure-particle velocity points chosen in this manner are plotted in Figure 8 together with a curve representing the best, least-squares fit to the data. The equation of the best fit line is also given in Figure 8.

## 2. Derivation of PUFF Code Inputs

An additional fit must be made to this data to obtain inputs compatible with the equation-of-state formulation used in the PUFF code; that is,

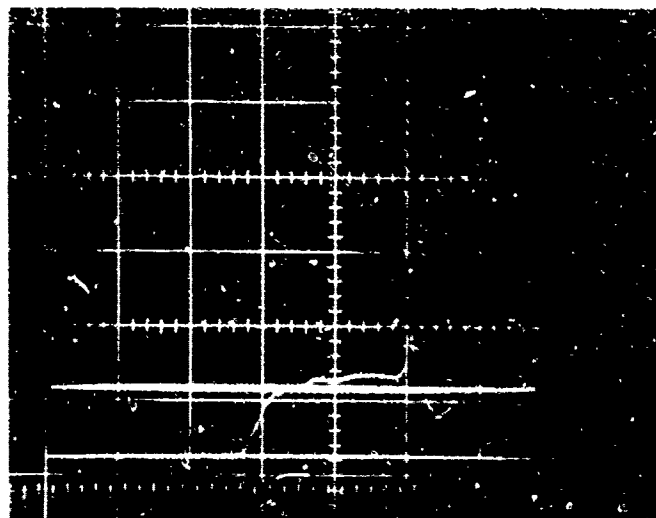
$$P = P_H(\mu) \left[ 1 - \frac{G\mu}{2} \right] + G\eta E, \quad (1)$$

$$\text{where } P_H(\mu) = C_H\mu + D_H\mu^2 + S_H\mu^3 \text{ (mb)}, \quad (2)$$

$$\mu = \frac{\rho}{\rho_0} - 1 = \eta - 1, \quad (3)$$

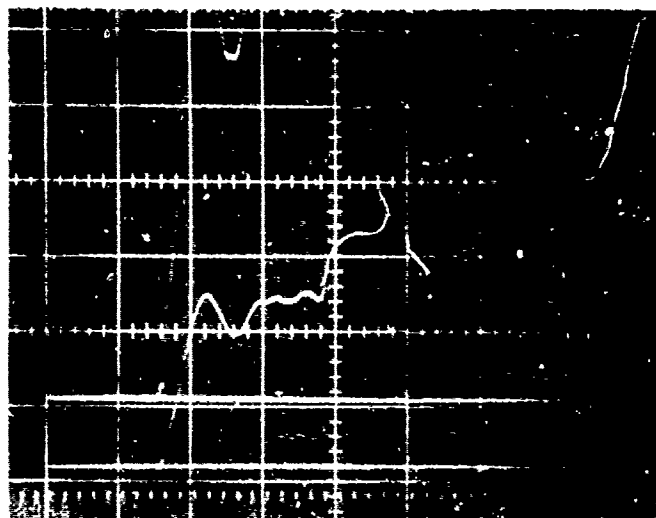


UPPER BEAM  
0.2  $\mu\text{S}/\text{CM}$   
LOWER BEAM  
0.5  $\mu\text{S}/\text{CM}$



SHOT NUMBER 1017

LOWER BEAM  
0.5  $\mu\text{S}/\text{CM}$

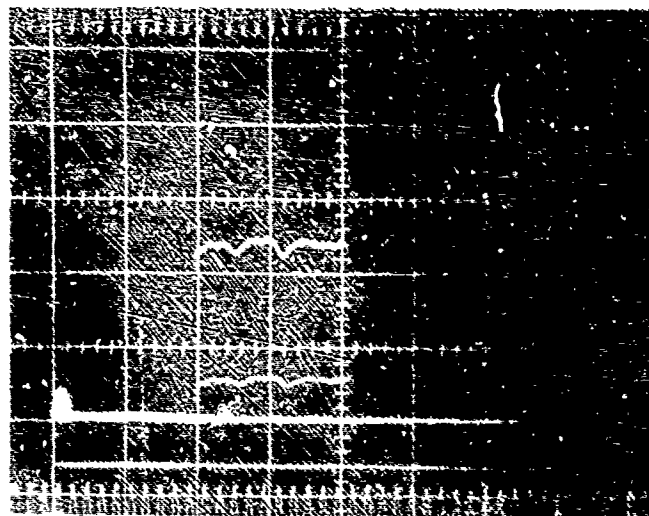


SHOT NUMBER 1034

FIGURE 3 EXPERIMENTAL RECORDS FROM TESTS 1017 AND 1034

UPPER BEAM  
0.5  $\mu$ S/CM

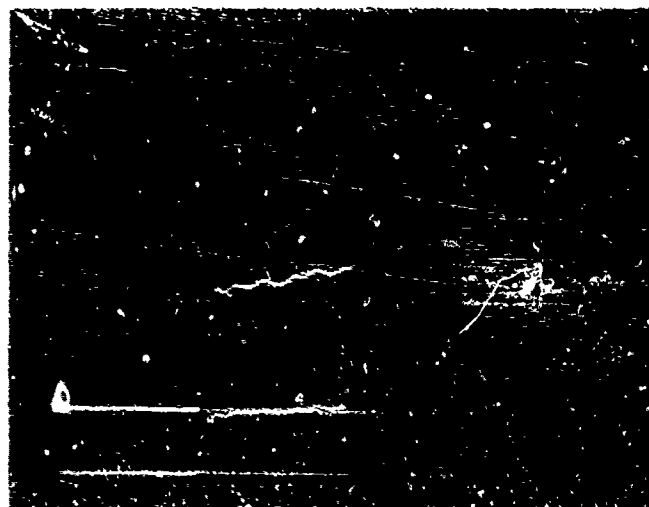
LOWER BEAM  
0.5  $\mu$ S/CM



SHOT NUMBER 1035

UPPER BEAM  
0.5  $\mu$ S/CM

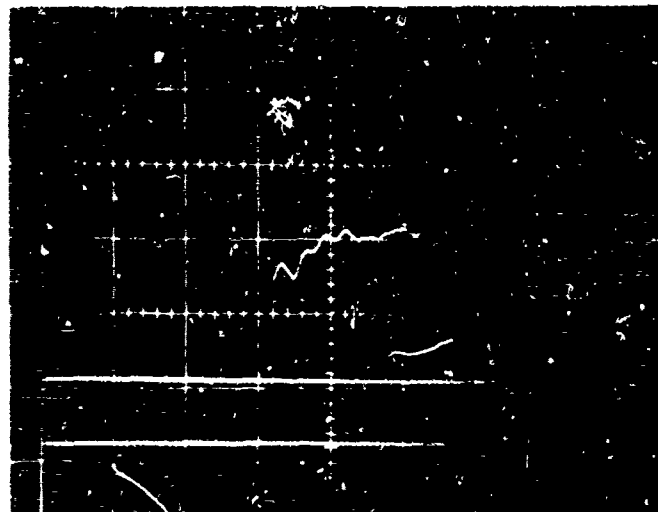
LOWER BEAM  
0.5  $\mu$ S/CM



SHOT NUMBER 1036

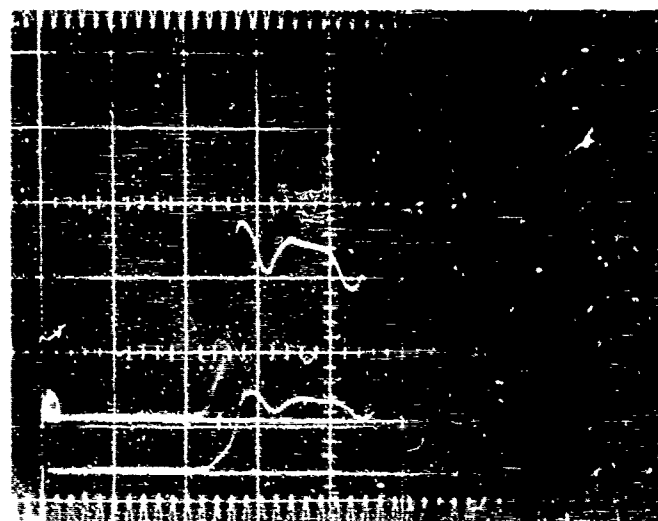
FIGURE 4 EXPERIMENTAL RECORDS FROM TESTS 1035 AND 1036

LOWER BEAM  
0.5  $\mu$ S/CM



SHOT NUMBER 1052

UPPER BEAM  
0.5  $\mu$ S/CM  
LOWER BEAM  
0.5  $\mu$ S/CM

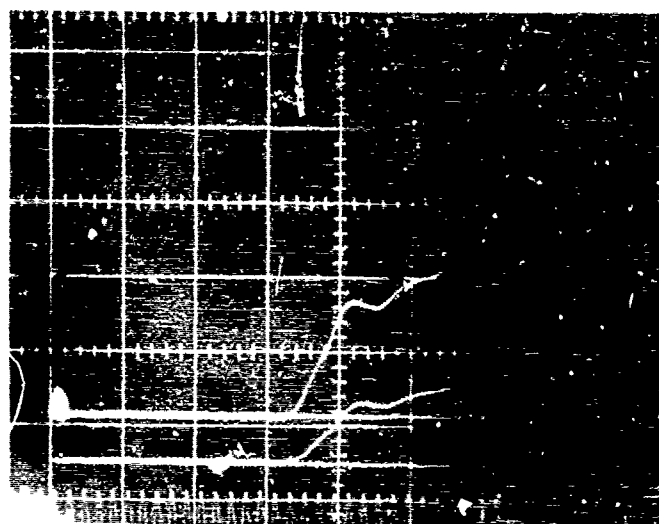


SHOT NUMBER 1053

FIGURE 5 EXPERIMENTAL RECORDS FROM TESTS 1052 AND 1053

UPPER BEAM  
0.5  $\mu$ S/CM

LOWER BEAM  
0.5  $\mu$ S/CM



SHOT NUMBER 1054

FIGURE 6      EXPERIMENTAL RECORD FROM TEST 1054

TABLE 1  
SUMMARY OF 3DCC HUGONIOT TESTS

SHOT NO.	IMPACT VELOCITY cm/ $\mu$ s	PEAK PRESSURE Kilobars	PEAK PARTICLE VEL. cm/ $\mu$ s
1017	0.03163	6.38	0.03101
1034	0.04498	15.8	0.04344
1035	0.06768	30.1	0.06475
1036	0.05406	21.6	0.05196
1040	-----	---NO DATA---	-----
1052	0.07223	30.9	0.06922
1053	0.02487	6.81	0.02421
1054	0.01181	2.07	0.01161

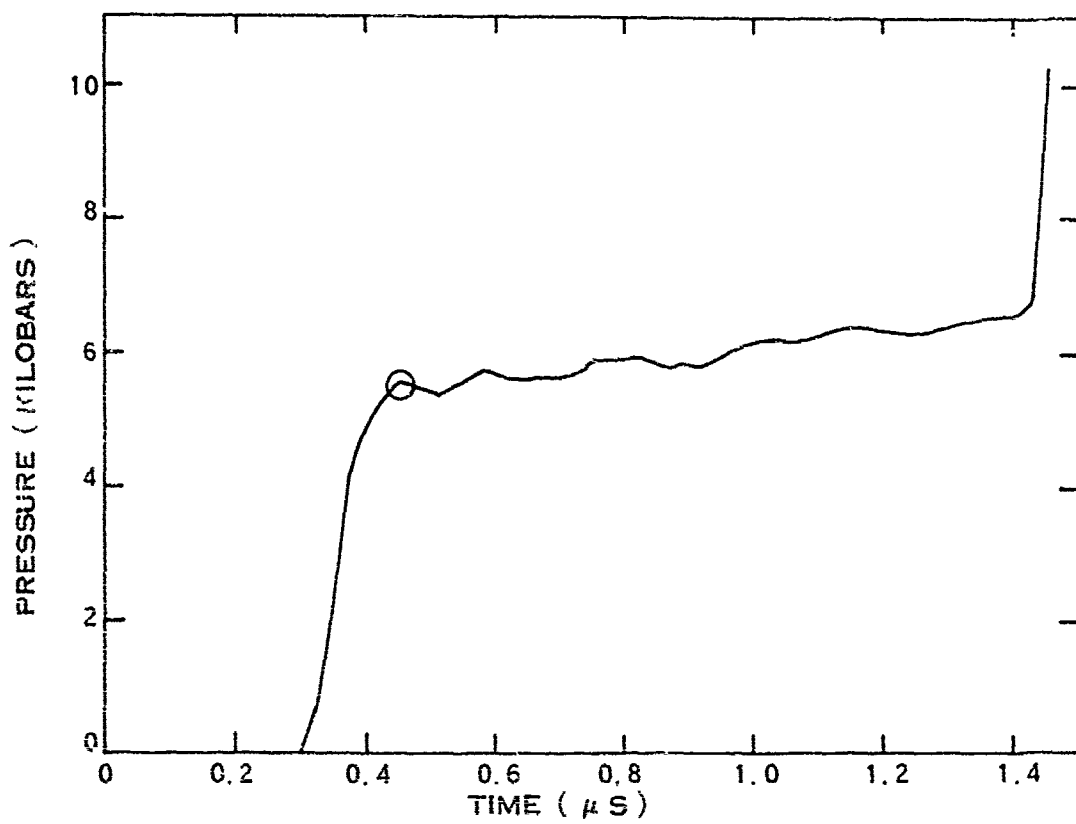


FIGURE 7 PEAK PRESSURE-PARTICLE VELOCITY POINT FOR TEST 1036

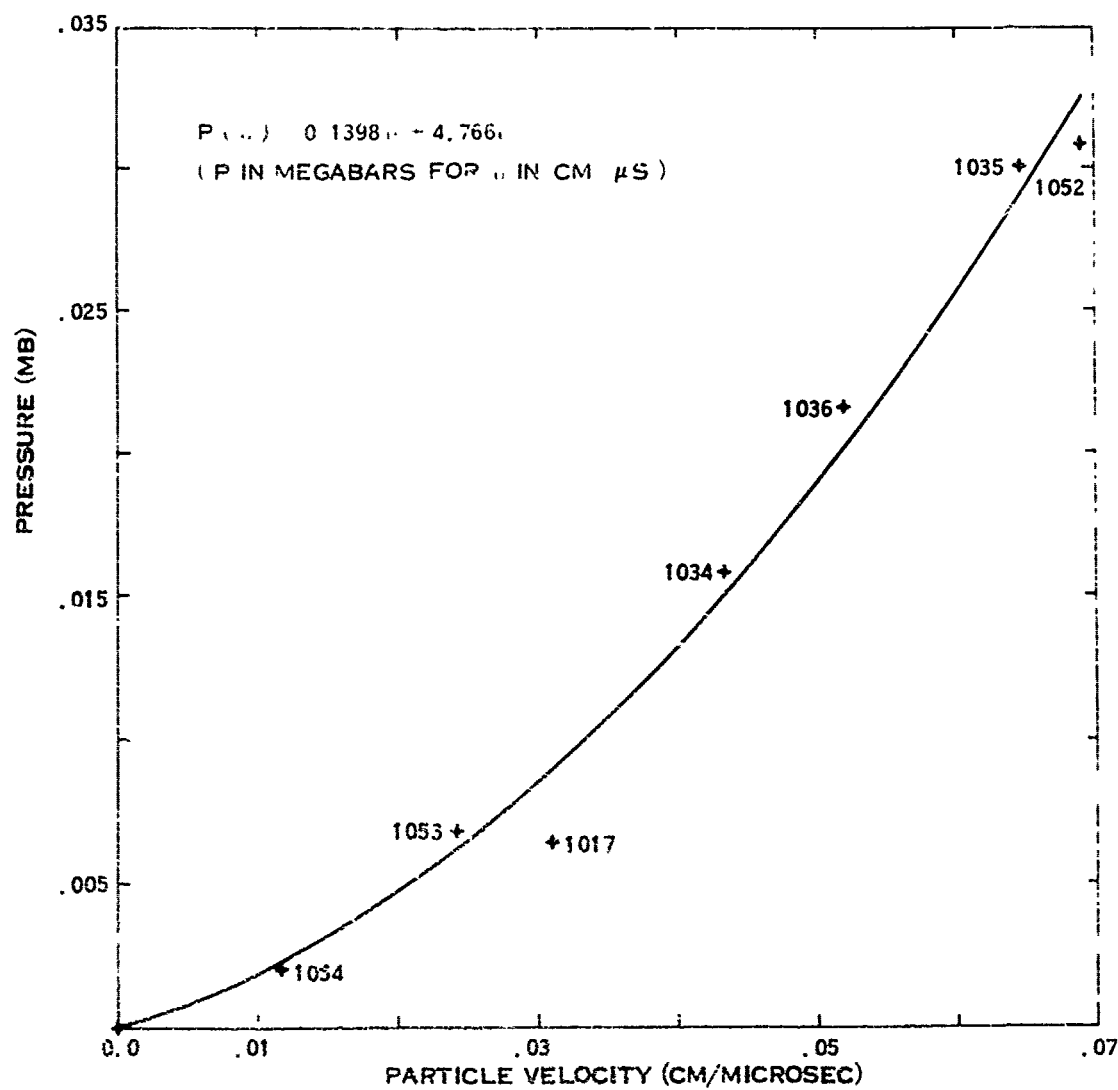


FIGURE 8 BEST FIT HUGONIOT CURVE FOR 3DCC

$E$  = internal energy (mb)

and,  $G$  = Grüneisen coefficient.

The coefficients  $C_H$ ,  $D_H$ , and  $S_H$  are determined from the Hugoniot data transformed from the  $P$ - $u$  to the  $P$ - $\mu$  plane using the following relationships derived from the Hugoniot jump conditions (see Appendix A, Equations A-22 and A-23).

$$U = \frac{P_H}{\rho_O u} \quad (4)$$

and,  $\mu = \frac{u}{U-u} \quad (5)$

where  $\rho_O$  = initial density,  $u$  = particle velocity, and  $U$  = shock velocity. Past experience indicates that the best way to accomplish the transformation and fit in  $P$ - $\mu$  for porous materials is to choose closely spaced points on the  $P$ - $u$  best fit line, convert these point by point to the  $P$ - $\mu$  plane using equations (4) and (5), then perform a least squares fit to the transformed points. This procedure minimizes the scatter of the data, as explained in Appendix B, under "Testing of Porous Materials".

Points from the  $P$ - $u$  fit for 3DCC, transformed by the above procedure to  $P$ - $\mu$  are shown in Figure 9 along with the best fit to the transformed points. The value of the initial density used for these transformations was  $\rho_O = 1.65 \text{ gm/cm}^3$ . This is the average value measured by Southern Research Institute on Advanced Heatshield Program (AHP) samples.

Examination of the  $P$ - $\mu$  fit of Figure 9 shows that the data implies a relationship not accurately describable by the cubic equation required by the PUFF code (Equation (2)). In order to improve the accuracy of the  $P$ - $\mu$  fit, several types



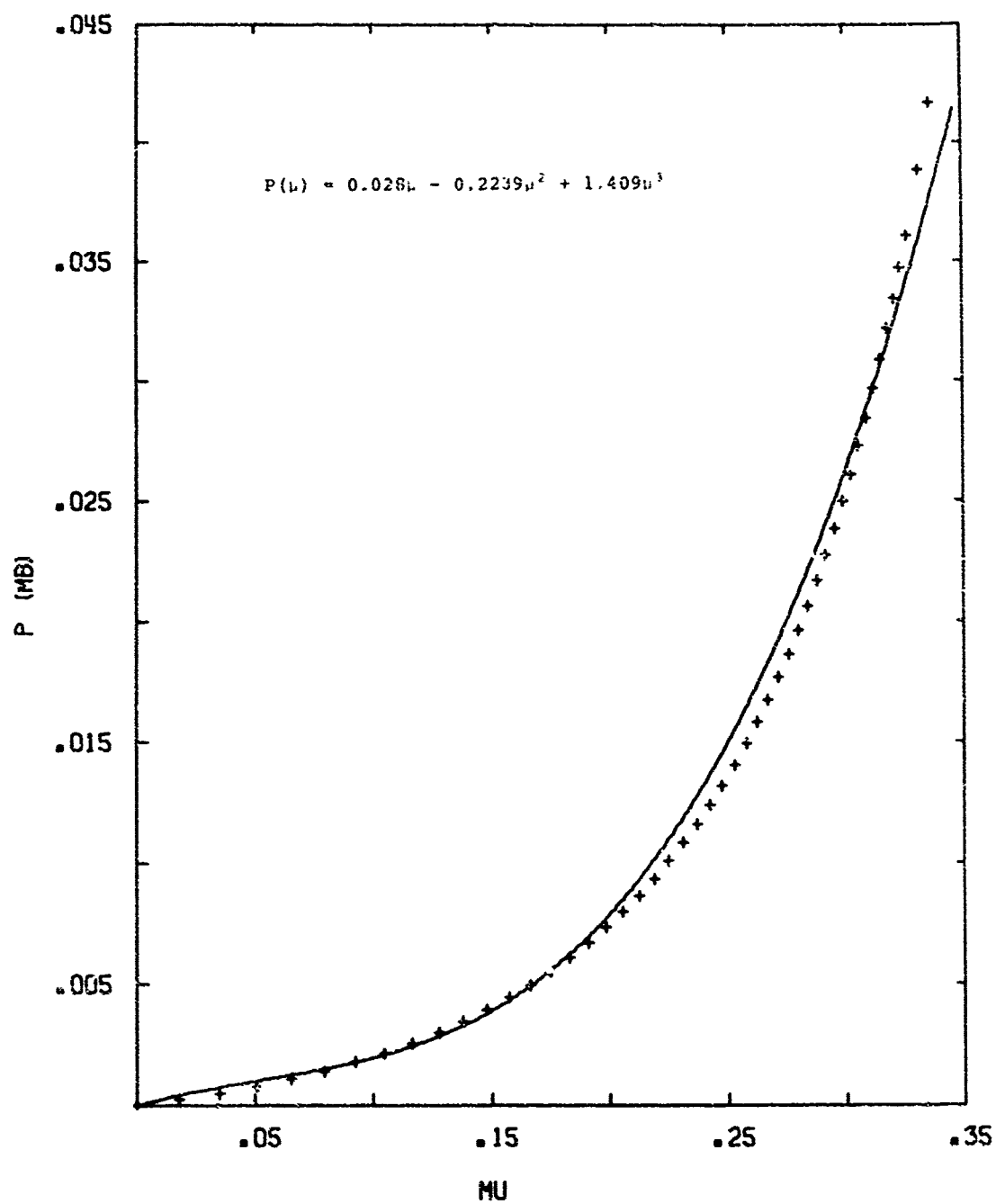


FIGURE 9 P- $\mu$  HUGONIOT FOR 3DCC

of functions were tried, with the best fit being obtained using the rational polynomial shown in Figure 10. This equation is not in suitable form for use in the PUFF code without modification of the code to accept the different form. In addition, the rational polynomial form is not good in the neighborhood of  $\mu = 0.45$ . Nevertheless, the fit is included here for completeness.

In summary, Hugoniot equation-of-state inputs for use with the PUFF code are:

$$\begin{aligned}C_H &= 0.028 \\D_H &= -0.2239 \\S_H &= 1.409 \\\rho_O &= 1.65 \text{ gm/cm}^3.\end{aligned}$$

If greater accuracy is desired, the rational polynomial fit shown in Figure 10 should be used.

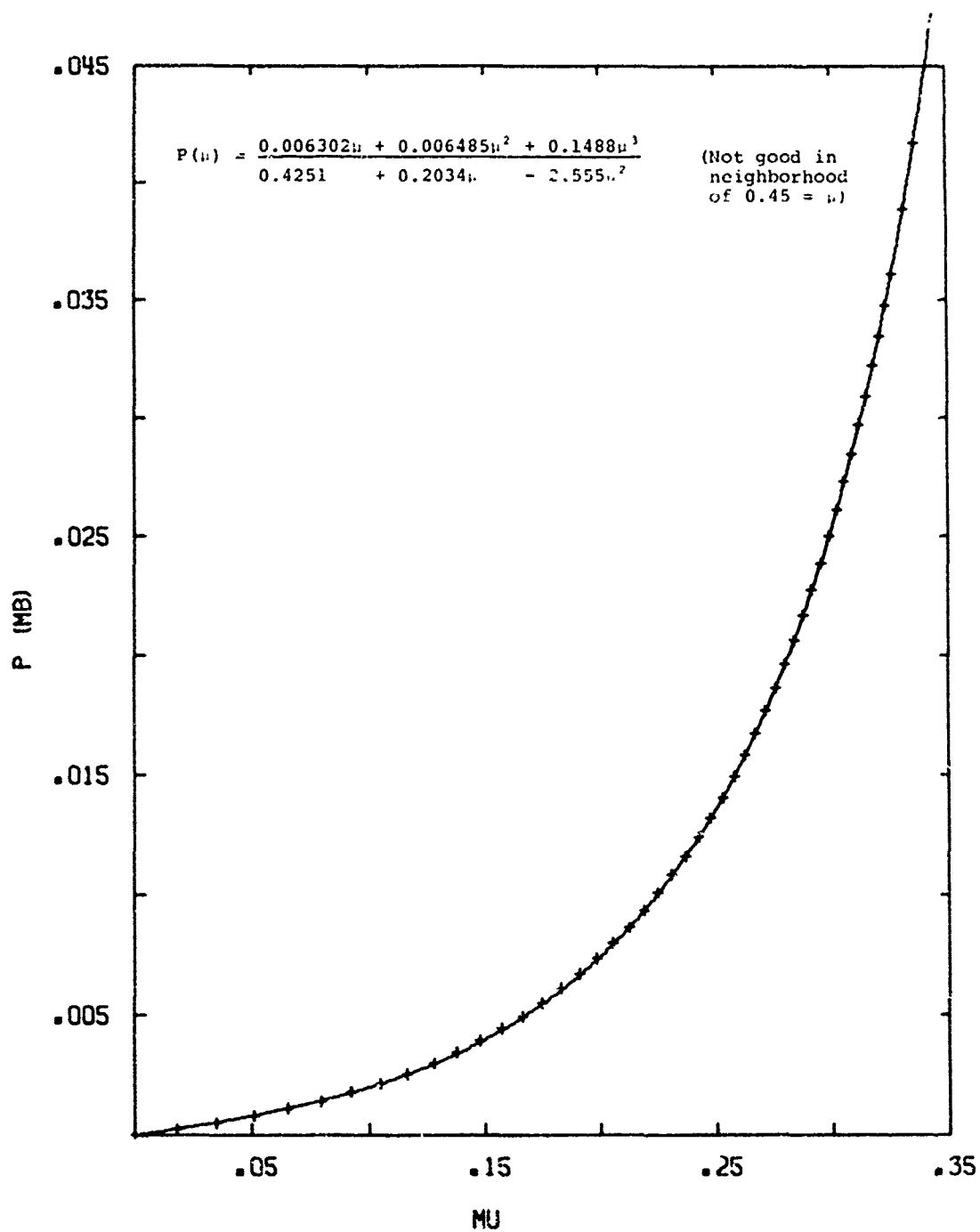


FIGURE 10 RATIONAL POLYNOMIAL P-μ FIT FOR 3DCC HUGONIOT

### SECTION III

#### WAVE ATTENUATION TESTING

##### 1. Sample Preparation and Test Procedure

After the Hugoniot testing, a second series of gas gun tests was performed on the AVCO 3DCC material to determine the stress wave attenuation characteristics of the material and to gather additional computer modeling data. Specimens of the AVCO 3DCC material were received from the manufacturer in the form of arcs cut from a 9.00-inch outside diameter cylindrical billet. The manufacturer's billet number was 1109-34. The samples were 1.5-inches in width by 1.5-inches in arc length and were 0.45-inch thick. Nominal density of the material was 1.65 gm/cc.

Additional machining of the samples, which consisted of grinding the specimens into a flat geometry, was performed at Kaman Sciences.

Early testing of this material at Kaman Sciences in support of the MISTY NORTH UGT event identified a two-wave structure in the transmitted waves through the material, with the wave velocities differing as much as a factor of three. This behavior is not attributed to conventional elastic-plastic response seen in metals but rather to a non-planar behavior with the radial fiber bundles passing disturbances much faster than either the matrix-lateral or lateral-lateral stacks. Disturbance velocities typical of the radial fiber bundles are also expected to exist along each lateral fiber bundle due to the commonality of fiber material. This required the samples to be reduced in

thickness and the edges to be potted in epoxy to permit the recording of attenuated waves before lateral relief produced two-dimensional strain fields at the recording surface. This problem was particularly acute in this case because manganin gages were selected to record the anticipated long duration transmitted stress. Manganin gages are very susceptible to producing erroneous stress output due to straining of the sensing element.

A schematic of the projectile-target geometry is shown in Figure 11. The manganin gages were installed between a 0.060-inch thick aluminum buffer plate and a 1-inch thick aluminum back-block and bonded to the rear of the 3DCC targets. (Previous calibration of this transducer assembly is described in Reference 1). Flat 3DCC targets were cut from the original arc specimens and mounted in the target holder such that impact would occur on the outer surface of the cylinder from which the arcs were cut. The samples were potted in Hysol 815 epoxy to provide a good impedance match at the sample-potting interface.

Thin 2024-T3 aluminum flyer plates of either 0.031-inch or 0.015-inch thickness were used to provide narrow pulse impacts and substantial stress wave attenuation across the targets. The thin flyers were supported with 1/8-inch cell aluminum honeycomb to prevent flyer distortion during launch. Each target assembly utilized a contact pin coupled with an electronic delay circuit to trigger oscilloscope sweep approximately at time of impact.

A variety of target thicknesses, flyer thicknesses and impact velocities were employed to provide a wide range

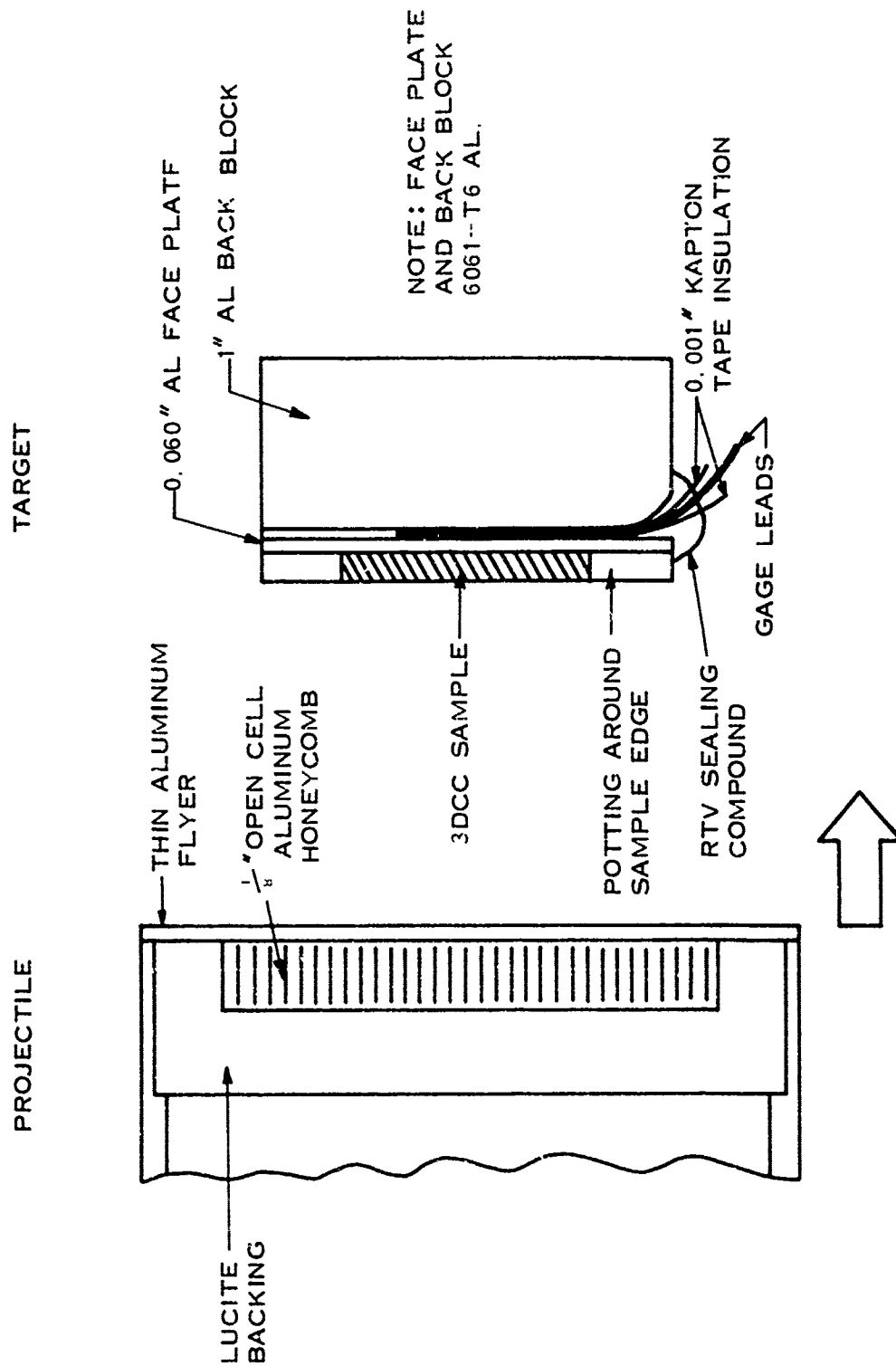


FIGURE 11 TEST CONFIGURATION FOR 3DCC TRANSMITTED WAVE TESTS

of input stress pulses and attenuation characteristics. Table 2 summarizes the results of the nine AVCO 3DCC attenuation experiments performed at KSC. In all cases, the attenuation ratio (defined as the impact stress divided by the back-face stress) across the samples was at least a factor of four and often much greater. Eight of the experiments utilized the flat impactor-target configuration shown in Figure 11. A ninth experiment, shot 1095, utilized a curved sample impacted by a curved flyer. The technique of impacting curved targets with curved flyers has been developed and widely used at Kaman Sciences, particularly for performing transmitted wave experiments with composite materials. In this case, however, the curved sample could not be potted on the edges in the same manner that the flat samples were and the recorded voltage output of the gage from shot 1095 gave evidence of lateral gage stretching and a resultant increase in resistance before the stress wave had completely passed the gage location. See Figure 12.

The reduced pressure versus time histories of the remaining eight attenuation experiments are shown in Figures 13 and 14. The recorded waveforms for all experiments show an initial, high velocity wave of less than 1 Kilo-bar amplitude running ahead of the main wave. In some of the experimental records, relief of the initial wave occurs before the arrival of the main wave. The initial wave is attributed to the characteristically high disturbance speeds of the radial fiber bundles. Relief of the initial wave is believed to be caused by either discontinuous motion in the radials, where the disturbance in the radial fiber bundles simply outdistances the main wave disturbance, or from relief waves emanating from the sample edges and interacting with a

TABLE 2  
3DCC STRESS WAVE ATTENUATION TESTS SUMMARY TABLE

SHOT NO.	FLYER	FLYER VELOCITY CM/ $\mu$ SEC	TARGET	IMPACT PRESSURE ~KBAR	PEAK GAGE PRESSURE ~KBAR	EST. BACKFACE PRESSURE ~KBAR
1089	.031" Aluminum	.068	.204" 3DCC	22.1	9.4	5.2
1090	.031" Aluminum	.068	.202" 3DCC	22.1	10.1	5.6
1091	.031" Aluminum	.068	.271" 3DCC	22.1	9.6	5.3
1093	.031" Aluminum	.044	.200" 3DCC	12.1	4.3	2.8
1095	.015" Aluminum	.045	.217" 3DCC	12.4	4.1	2.7
1096	.015" Aluminum	.043	.200" 3DCC	11.8	3.4	2.2
1097	.015" Aluminum	.050	.330" 3DCC	14.5	3.5	2.3
1098	.015" Aluminum	.054	.200" 3DCC	16.2	2.7	1.8
1099	.015" Aluminum	.068	.326" 3DCC	22.1	6.9	4.1



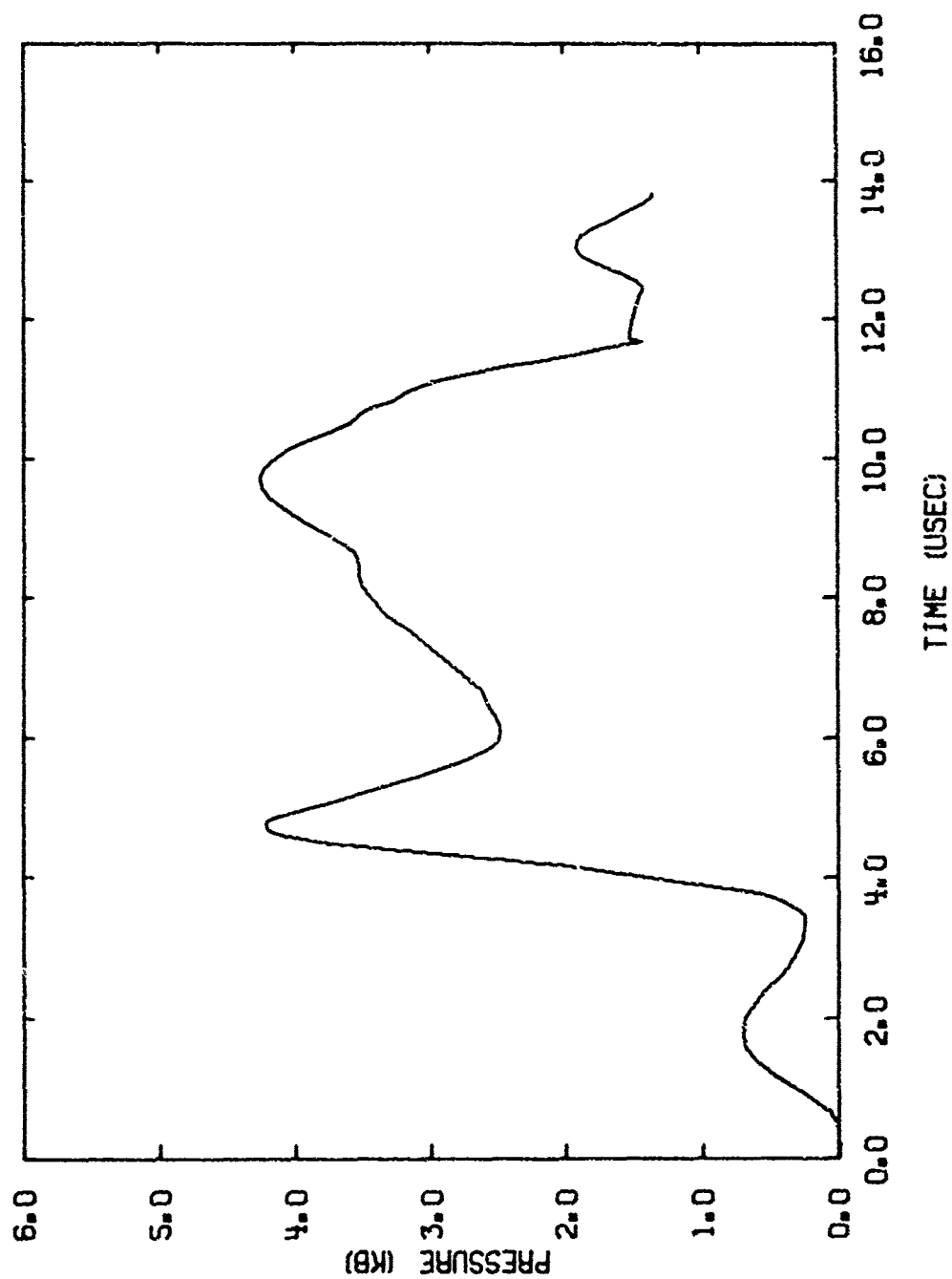


FIGURE 12 EXPERIMENTAL RECORD FROM TEST 1095

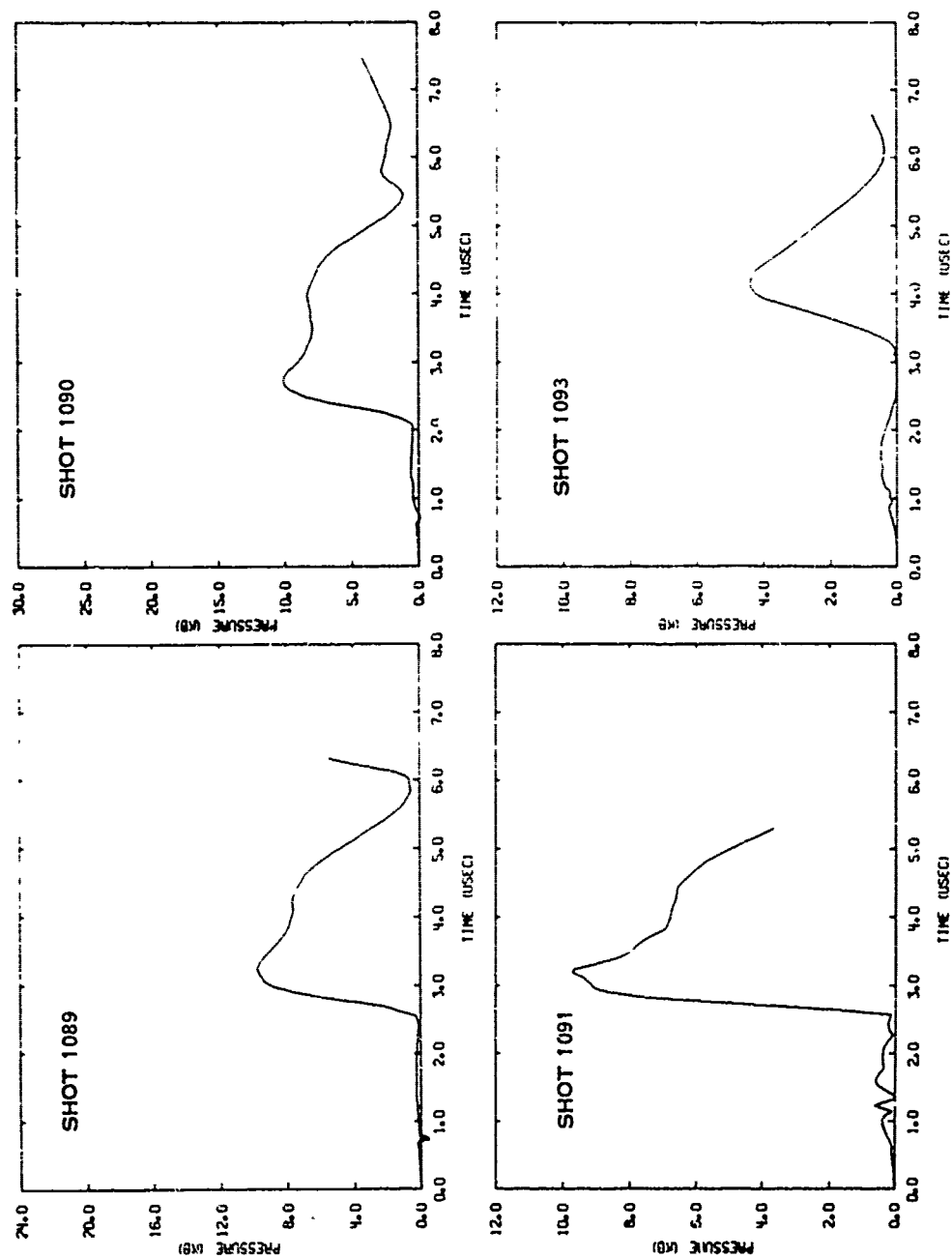


FIGURE 13 3DCC WAVE PROFILE MEASUREMENTS

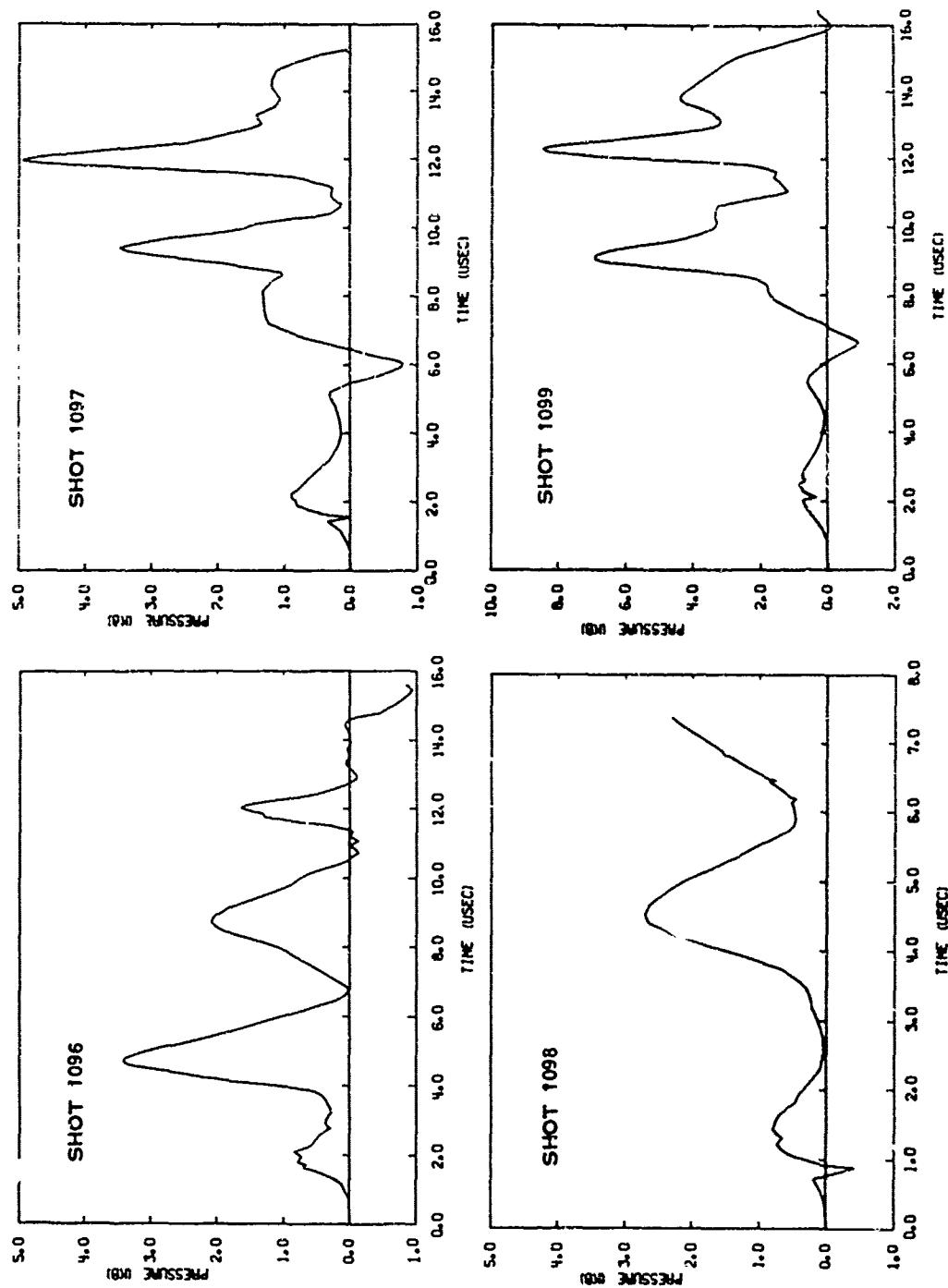


FIGURE 14 3DCC WAVE PROFILE MEASUREMENTS

continuous initial wave. Rise times of the main waves generally varied from 200 nanoseconds to 1 microsecond. The longer rise times are attributed to internal pre-test delaminations. These delaminations have been observed at Kaman using radiographic techniques and appear as small, complete separations parallel to the major surfaces of the manufactured part. The shorter rise times of 200 nanoseconds would preclude geometric dispersion from being a major factor in attenuation of the stress waves.

## 2. Computer Code Correlation

Correlation of the AVCO 3DCC attenuation experiments has been attempted using a P- $\alpha$  constitutive foam crushing model. The P- $\alpha$  constitutive model of Hermann (References 2 and 3) is an irreversible compaction model which includes a limited amount of reversible elastic behavior. The Hugoniot data of Section II has been used to construct a loading path and a crush curve for the AVCO 3DCC material. Unloading behavior of the P- $\alpha$  model is determined from the elastic wave velocity (in this case the radial fiber bundle disturbance velocity) and the reference, fully compacted, Hugoniot. Unloading velocities vary linearly between these two limits. The reference, fully compacted, Hugoniot is taken to be that of pyrolytic graphite with a crystalline density of 2.25 gm/cc.

The experimental Hugoniot data and the reference Hugoniot are shown in pressure-volume coordinates in Figure 15. The highest pressure (~30 Kbar) data point did not result in complete compaction of the material. An elastic velocity of 0.47 cm/ $\mu$ sec has been determined from the wave

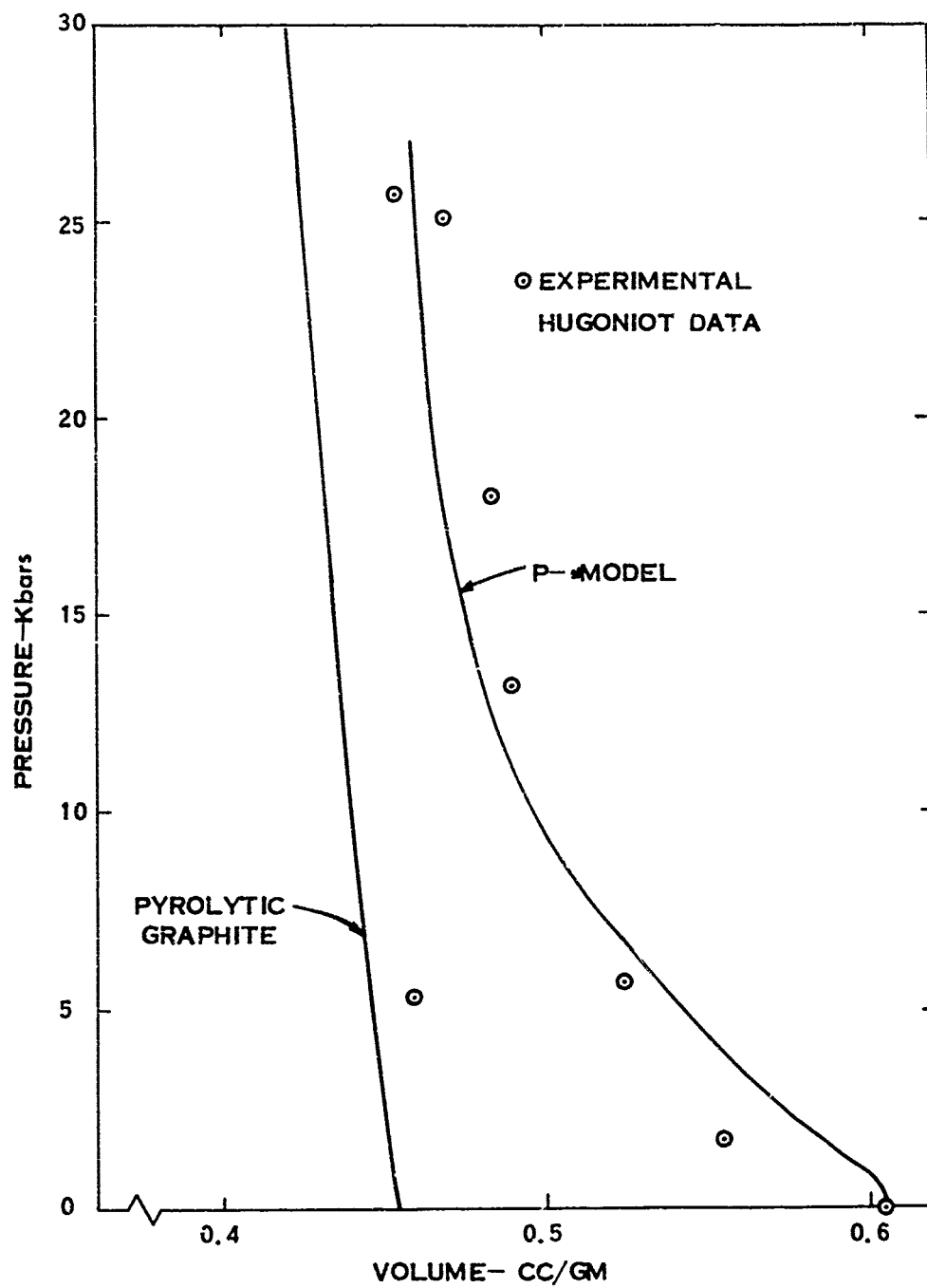


FIGURE 15 AVCO 3DCC EQUATION OF STATE

attenuation experiments. A velocity this large would suggest that the initial wave cannot be overdriven, but instead would be present in all experimental situations. A quadratic P- $\alpha$  crush curve has been used to fit the experimental Hugoniot data starting from an elastic limit of 0.5 Kilobar.

Of the nine wave attenuation experiments performed, four have been subjected to hydrocode correlations using the P- $\alpha$  response model. The correlations were performed for shot numbers 1089, 1090, 1096, and 1098. The flyer plate impact was recreated with the code using the impact conditions described in Table 2 and approximating the honeycomb supported rear face of the flyer as a free surface. The experimental-analytical correlations are shown in Figures 16 through 18. Target thicknesses on all four experiments were nominally 0.2-inch. Experiments 1089 and 1090 employed 0.031-inch thick aluminum flyers; whereas both 1096 and 1098 used the thinner 0.015-inch thick aluminum flyers. The thicker 0.031-inch flyer produces an input pulse width of approximately 250 nano-seconds per flyer reverberation.

The hydrocode correlation with experiments 1089 and 1090 produced very good agreement on both wave velocities and amplitudes. The slight underprediction of peak main wave amplitude is seen on both experiments. Analytical correlations with the thinner flyer plate experiments (shot numbers 1096 and 1098) does not produce as good agreement, particularly for the wave velocities. The initial precursor wave (believed to have its origin in predominantly radial fiber bundle motion) appears to travel much faster in the thinner flyer plate experiments. An additional factor may be that the P- $\alpha$  crush curve established for the AVCO 3DCC

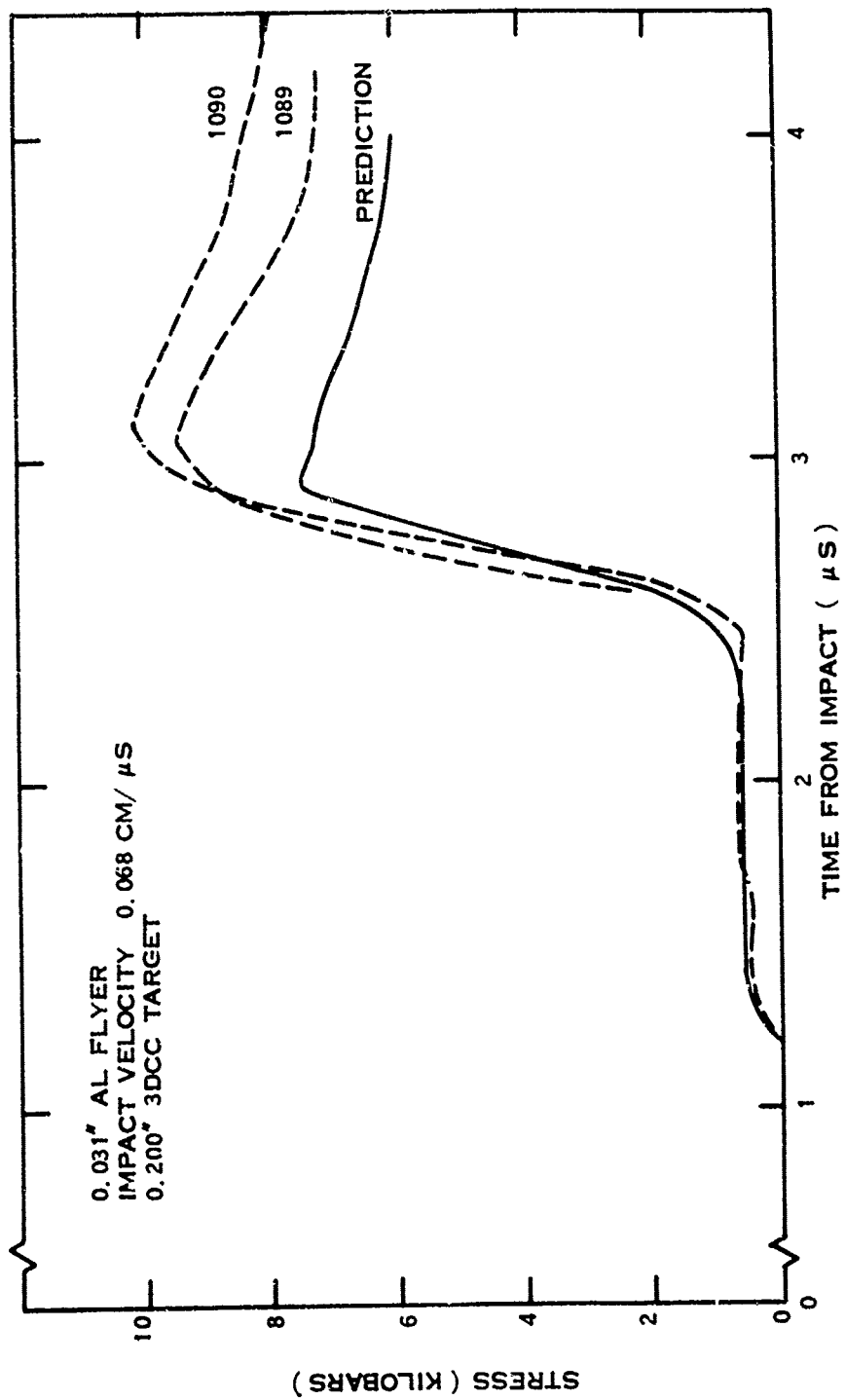


FIGURE 16 WAVE PROFILE COMPARISON FOR TESTS 1089 AND 1090

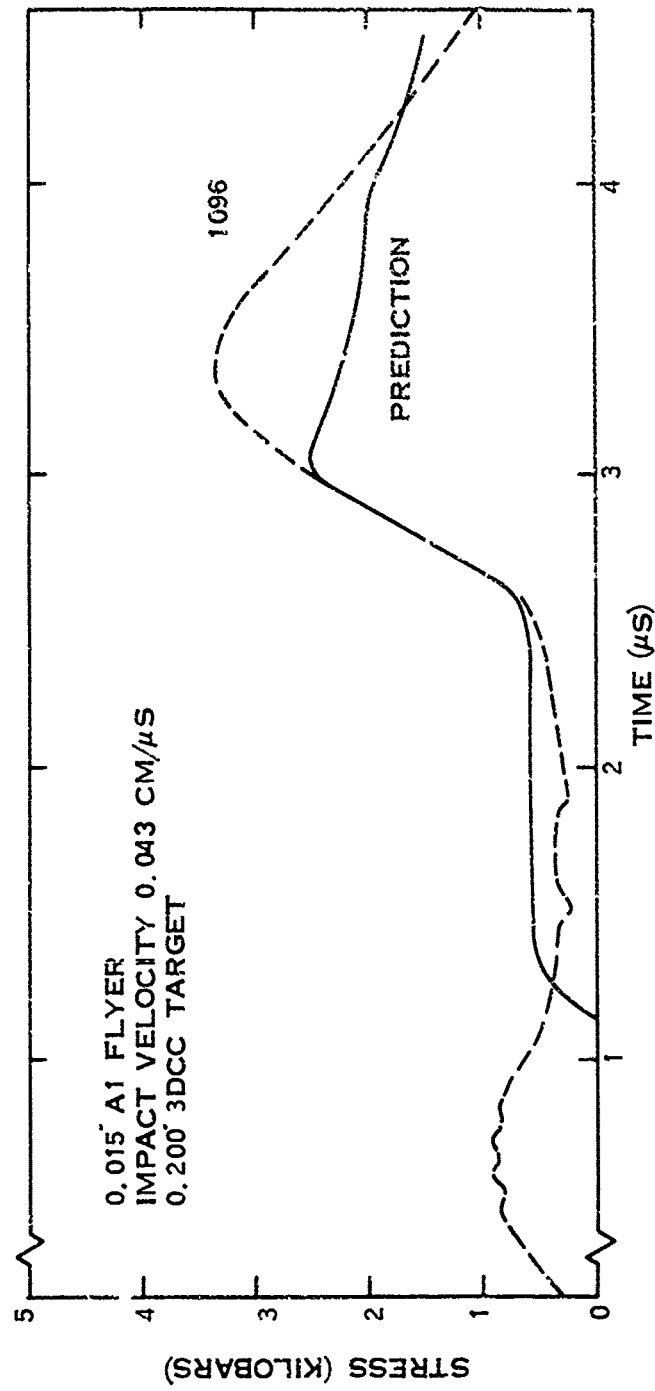


FIGURE 17 WAVE PROFILE COMPARISON FOR TEST 1096



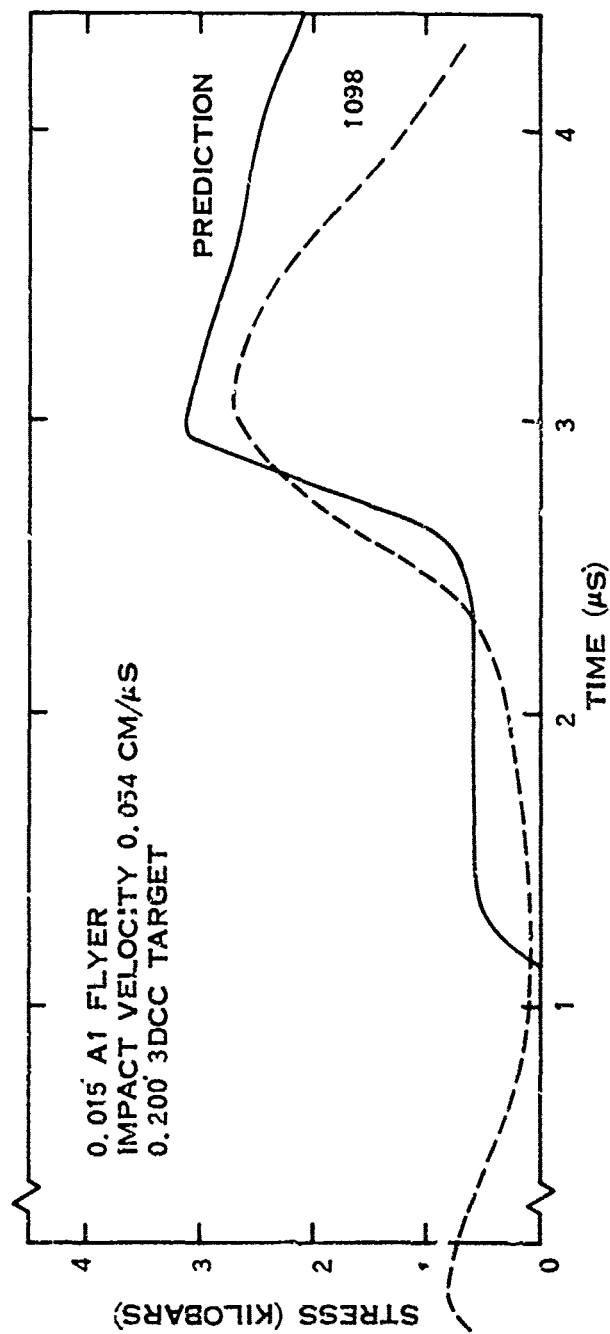


FIGURE 18 WAVE PROFILE COMPARISON FOR TEST 1098

material may deviate substantially from the experimentally observed material crushing behavior at the lower stresses; thereby producing higher compaction wave velocities in the analytical solutions. Inspection of the  $P-\alpha$  curve fit to the experimental Hugoniot data (Figure 15) indicates that the chosen  $P-\alpha$  curve fit may not be optimum for the lower stress region.

The attempted hydrocode correlations of the wave attenuation experiments of the AVCO 3DCC material have shown that the Hermann  $P-\alpha$  dynamic compaction model is a suitable analog of the actual material behavior and can be used with confidence to predict stress wave response in this material. The weakness of the model lies in its assumption of planar motion in both the precursor and main shock waves. This assumption may be correct for the main, or compaction, wave but the motion in the initial wave is believed to be highly non-planar, involving predominantly motion in the radial fiber bundles with only slight mechanical coupling with the remaining material.

#### LIST OF REFERENCES

1. Bobby L. Bracewell, Thomas F. V. Meagher, "Material Characterization and Transducer Evaluation for MISTY NORTH Pressure Measurements", AFWL-TR-72-224, May 1973.
2. W. Herrmann, "Equation of State of Crushable Distended Materials", Sandia Document SC-RR-66-2678, March 1968.
3. W. Herrmann, "On the Elastic Compression of Crushable Distended Materials", Sandia Document SC-DR-68-321, June 1968.

## APPENDIX A

### THEORETICAL BACKGROUND

The purpose of this appendix is to briefly review the theoretical background and analytical methods which must be used in connection with experimental measurements in order to understand and describe the behavior of solid materials under high pressure, shock wave loading.

The theory described below will be concerned only with plane shock waves propagating in the positive x-direction. The material is considered to be infinitely wide in order to avoid complications arising from reflections at boundaries. This situation is approximated in the laboratory by using a test geometry with lateral dimensions which are large compared to the longitudinal dimension. In addition, the states of the material both before and after the passage of the shock wave are considered to be states of thermodynamic equilibrium, and in a frame of reference in which the shock transition region is stationary; the velocity of the material moving toward the transition region must be supersonic and moving away from the transition region must be subsonic. (This last criterion distinguishes a shock transition from a Joule-Thomson expansion in which the flow velocity is always subsonic).

#### 1. Theoretical Description of Shock Behavior

At pressures high compared to the yield strengths of solids, it is customary, as a first approximation, to assume that a material behaves as a perfect fluid. The equations of motion for such a material are derived by assuming only

the basic principles of conservation of mass, momentum, and energy (Reference A-1). The special equations for uniaxial strain, which is the condition of most interest here, are best expressed in the Lagrangian coordinate system. In this system, spatial coordinates are fixed in the medium and undergo all the motion experienced by the medium. Thus, for one-dimensional motion, the coordinate  $x$  represents the position of a particular particle of the material, and can be expressed as a function of the time  $t$  and some characteristic parameter, such as the initial value of  $x$ .

The equations of motion are then:

$$\text{Conservation of mass: } \frac{\partial \rho}{\partial t} + \rho \frac{\partial u}{\partial x} = 0 \quad (\text{A-1a})$$

$$\text{Conservation of momentum: } \rho \frac{\partial u}{\partial t} + \frac{\partial P}{\partial x} = 0 \quad (\text{A-1b})$$

$$\text{Conservation of energy: } \frac{\partial E}{\partial t} + P \frac{\partial}{\partial t} \left( \frac{1}{\rho} \right) = \frac{\partial Q}{\partial t} \quad (\text{A-1c})$$

where

$\rho$  = material mass density

$u$  = particle velocity

$P$  = pressure

$E$  = internal energy per unit mass

$Q$  = internal energy source term.

Equations (A-1) are the basic differential equations (neglecting viscosity) of elementary fluid dynamics. When the necessary initial and/or boundary conditions are given, these equations can be used, along with an appropriate equation-of-state to completely describe the fluid motion. The equation-of-state is usually best expressed in the form

$$P = P(\rho, E). \quad (A-2)$$

In general, an analytical solution of the non-linear Equations (A-1) and (A-2) is not possible, even though useful numerical solutions can be obtained. In addition, it is assumed in the development of Equations (A-1) that all the dependent variables  $\rho$ ,  $u$ ,  $P$ ,  $E$  and  $Q$  can be expressed as continuous functions of the Lagrangian variable  $x$  and the time variable  $t$ . However, in the case of a shock wave, the wave front steepens during propagation and eventually forms an interface across which approximate discontinuities in the dependent variable occur. Since derivatives do not exist at such discontinuities, Equations (A-1) must be replaced in this region by a new set of relationships based on the same physical conservation laws.

Applying the conservation laws across the shock front leads to the so-called jump conditions (References A-1, A-2, and A-3).

$$\text{Conservation of mass:} \quad \rho_0 U = \rho (U - u) \quad (A-3a)$$

$$\text{Conservation of momentum:} \quad P - P_0 = \rho_0 U u \quad (A-3b)$$

$$\text{Conservation of energy:} \quad P u = \rho_0 U (E - E_0 + u^2/2) \quad (A-3c)$$

where  $U$  is the shock velocity,  $u$ ,  $P$ ,  $V$ ,  $\rho = 1/V$ , and  $E$  are the particle velocity, the pressure, the specific volume, the density, and the specific internal energy of the material behind the shock front and  $P_0$ ,  $V_0$ ,  $\rho_0 = 1/V_0$ ,  $E_0$  are the values of these quantities ahead of the shock front (in this case,  $u_0 = 0$ ).

The elimination of  $U$  and  $u$  from Equation (A-3c) yields the Rankine-Hugoniot relation

$$E - E_0 = (P + P_0)(V_0 - V)/2 \quad (A-4)$$

that defines all states on the  $(E-P-V)$  surface that can be reached from an initial condition  $(E_0, P_0, V_0)$  by a single shock transition. If the  $E(P,V)$  equation-of-state is known, Equation (A-4) defines the locus of shocked states as a curve in the  $(P-V)$  plane

$$P = P_H(P_0, V_0, V) \quad (A-5)$$

which passes through the initial state  $(P_0, V_0)$  and is called the Hugoniot curve centered at  $(P_0, V_0)$ . The entropy increases along the Hugoniot curve as the pressure increases because the shock is irreversible (Reference A-1). It is important to keep in mind that the Hugoniot curve is not a "process" curve. That is, it does not represent a series of equilibrium states the material would traverse in changing from the initial state  $(P_0, V_0)$  to some other state  $(P, V)$ . It is rather the locus of possible end states  $(P, V)$  which can be attained in the material by shock transition from the initial state  $(P_0, V_0)$ . Each point on the Hugoniot curve must be obtained by a separate experiment. The Hugoniot curve by itself gives no information about what type of path is followed in the  $(P-V)$  plane as the material goes from  $(P_0, V_0)$  to  $(P, V)$ , although it is sometimes used for this purpose as a first approximation in computations.

The elimination of  $u$  from Equations (A-3a) and (A-3b) gives

$$P - P_0 = (U/V_0)^2 (V_0 - V) \quad (A-6)$$

the equation of a straight line that is called the Rayleigh line. Because the shocked state must satisfy Equations (A-5) and (A-6), the intersection of the Hugoniot curve centered at  $(P_0, V_0)$  defines the thermodynamic state  $(P, V)$  behind a shock traveling with constant velocity  $U$  in a stationary material with pressure  $P_0$  and specific volume  $V_0$ . Figure A-1 illustrates the relationship in the  $(P, V)$  plane of the curves described by Equations (A-5) and (A-6) to two "process" curves, the adiabat (or isentrope, for a reversible process) and the isotherm (References A-1 and A-3).

Examination of Equations (A-3) and (A-4) will point out that shock wave measurements yield what may be called an  $E(P, V)$  incomplete equation-of-state, since only the thermodynamic variables  $P$ ,  $V$ , and  $E$  are computed from the jump conditions. The variables specific entropy  $\phi$  and temperature  $T$  are not involved explicitly in the equations. As a result, neither the values of  $\phi$  and  $T$  along a Hugoniot curve nor values of the state variables off a Hugoniot curve can be calculated solely from Hugoniot data. The assumptions which are usually made in order to obtain a more complete thermodynamic description of a material (consistent with Hugoniot measurements) are described in Part 2 below. The development follows that given in Reference A-4.

## 2. Basic Thermodynamics of Shock Waves

### a. The Equation-of-State

The term "equation-of-state" has unfortunately been used in shock wave literature to denote a variety of relationships which convey different amounts of thermodynamic information about the system under consideration. Quite frequently



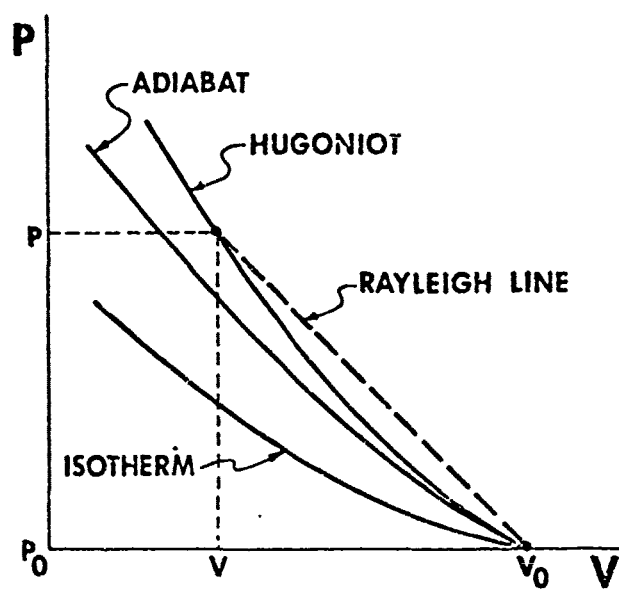


FIGURE A-1

COMPARISON OF VARIOUS CURVES IN THE  $(P-V)$  PLANE

curves such as isentropes, adiabats, or Hugoniot are referred to as equations-of-state. The specification of one of these curves is not a specification of the equation-of-state of the system because the equation-of-state is a function of at least two independent variables.

In a simple, nonreacting, single phase system, the two independent variables are generally taken to be any two of the four variables specific volume, pressure, temperature, and entropy, denoted by  $V$ ,  $P$ ,  $T$ , and  $\phi$  respectively. Expressions for the remaining two as functions of the two so chosen constitute a complete equation-of-state, since they yield a complete thermodynamic description of the system. Each of the relationships independently is called an incomplete equation-of-state. For example, given the two relationships  $T = T(\phi, V)$  and  $P = P(\phi, V)$  (which can in principle be inverted so that any pair of variables is independent), the internal energy can be found from

$$dE = \frac{\partial E}{\partial \phi} d\phi + \frac{\partial E}{\partial V} dV. \quad (A-7)$$

Since

$$T(\phi, V) = \left( \frac{\partial E}{\partial \phi} \right)_V \text{ and } P(\phi, V) = - \left( \frac{\partial E}{\partial V} \right)_\phi \quad (A-8)$$

then

$$dE = Td\phi - PdV. \quad (A-9)$$

Knowledge of the internal energy  $E(\phi, V)$  is then seen to be equivalent to the two equations-of-state  $T(\phi, V)$  and  $P(\phi, V)$ . The function  $E(\phi, V)$  is frequently called a fundamental equation or complete equation-of-state because it also

contains a complete thermodynamic description of the system. Similarly, the Helmholtz free energy  $F(V,T)$ , the enthalpy function  $H(\phi,P)$ , and the Gibbs free energy  $G(P,T)$  serve as fundamental equations when the independent variables are the pairs  $(V,T)$ ,  $(\phi,P)$ , and  $(P,T)$  respectively.

A frequently occurring incomplete equation-of-state is the internal energy  $E(V,T)$  or  $E(P,V)$ . Since the internal energy is a complete equation-of-state or fundamental equation only when it is expressed as a function of  $\phi$  and  $V$ , then if  $E(V,T)$  is known, supplementing it with either  $P(V,T)$  or  $\phi(V,T)$  constitutes a complete equation-of-state. (Note that in the latter case,  $\phi(P,V)$  or  $P(\phi,V)$  or  $V(\phi,P)$  is equivalent since the expressions in principle can be inverted so that any pair of variables is independent.)

#### b. Mie-Grüneisen Equation-of-State

In shock wave research, the incomplete equation-of-state  $E(P,V)$  is of particular interest. A Hugoniot curve is obtained by subjecting an  $E(P,V)$  incomplete equation-of-state to the constraint

$$E(P,V) = E_0 + (P_0 + P)(V_0 - V)/2 \quad (A-10)$$

where  $E_0 = E(P_0, V_0)$  and  $P$  and  $V$  are values along the Hugoniot curve. Specifying the Hugoniot curve is not specifying an equation-of-state of the system since the values of  $P$ ,  $V$ , and  $E$  are computed from the jump conditions expressing the conservation of mass, momentum, and energy that do not involve the entropy and temperature explicitly. Hence, neither  $\phi$  and  $T$  along the Hugoniot nor  $(P,V,E)$  states off the Hugoniot can be determined using only the jump conditions. One method

of making the thermodynamic description obtainable from a Hugoniot curve more complete is to assume a (P-V-E) equation-of-state which allows calculation of (P,V,E) states bordering the Hugoniot. The Mie-Grüneisen (P-V-E) equation-of-state with the Grüneisen ratio  $\Gamma$  assumed to be a function of volume only has been used for this purpose with some success.

In general, the Grüneisen parameter, as for all thermodynamic state variables, is a function of two independent variables and is defined by

$$\Gamma(X,Y) = V \left( \frac{\partial P}{\partial E} \right)_V = V \frac{(\partial P / \partial T)_V}{(\partial \Sigma / \partial T)_V} = V \frac{(\partial \Phi / \partial V)_T}{T (\partial \Phi / \partial T)_V} \quad (A-11)$$

where X and Y represent any two of the five variables E, P,  $\Phi$ , V, and T which are chosen as independent. The generalized Mie-Grüneisen equation-of-state may be defined as the solution of any one of the partial differential equations of Equation (A-11) when  $\Gamma(X,Y)$  is specified. All of the definitions of Equation (A-11) are equivalent and may be derived one from another by applying thermodynamic identities. The usual Mie-Grüneisen equation-of-state as applied to solids can be derived from at least two different sets of assumptions. In the first case, the equation-of-state follows from the assumption that the distortional and vibrational energy in a lattice solid are separable and from some simplifying assumptions about the lattice spectrum; e.g., that it follows the Debye or Einstein model (Reference A-2). In the second case, the equation-of-state is assumed to be an analytical function of volume and vibrational energy. In addition, the material is assumed to sustain a finite pressure at zero degrees Kelvin, and the Grüneisen parameter is taken to be a function of volume only,  $\Gamma = \Gamma(V)$ . Then a series expansion

in  $V$  and  $E$  leads directly to the Mie-Grüneisen equation-of-state

$$P - P_C(V) = \frac{\Gamma(V)}{V} [E - E_C(V)] \quad (A-12)$$

if only the first order term in  $E$  is retained. The point  $P, V, E$  refers to any arbitrary equilibrium state in the region of the pressure-volume plane for which Equation (A-12) is valid.  $P_C(V)$  and  $E_C(V)$  are the compressional pressure and energy at the same volume. Equation (A-12) says, then, that at volume  $V$  the thermal component of the pressure,  $P - P_C(V)$ , is equal to  $\Gamma(V)/V$ , a function of volume, times the thermal component of the energy at the same volume. In particular, if the pressure-volume-energy state under consideration lies on the Hugoniot curve centered at  $P_O, V_O, E_O$ , Equation (A-12) becomes

$$P_H - P_C(V) = \frac{\Gamma(V)}{V} [E_H - E_C(V)] \quad (A-13)$$

Subtraction of Equation (A-12) from Equation (A-13) yields

$$P - P_H = \frac{\Gamma(V)}{V} [E - E_H] \quad (A-14)$$

Equation (A-14) now says that at volume  $V$  the difference in thermal pressure between the state  $P, V, E$ , and the Hugoniot centered at  $P_O, V_O, E_O$  is equal to  $\Gamma(V)/V$  times the difference in thermal energy between state  $P, V, E$  and the Hugoniot. It is convenient to use the equation-of-state in the form of Equation (A-14) with the Hugoniot as a reference.

If  $\Gamma(V)$  is assumed to have a constant value  $G$  and the experimental Hugoniot is expressed as a function of  $\mu = (V_O/V) - 1$ , Equation (A-14) can be written

$$P = P_H(\mu) + G\rho E' \quad (A-15)$$

where  $\rho = 1/V$  and  $E' = E - E_H$ , the thermal energy offset from the Hugoniot. The Hugoniot internal energy and pressure are related through

$$E_H = E_O + P_H(V_O - V)/2 = E_O + \frac{\mu P_H}{2\rho} \quad (A-16)$$

Substitution of Equation (A-16) into (A-15) yields

$$P = P_H(\mu) \left[ 1 - \frac{G\mu}{2} \right] + G\rho(E - E_O) \quad (A-17)$$

where  $E$  is the total internal energy and  $E_O$  is the internal energy at the foot of the Hugoniot  $P_H(\mu)$ . Equation (A-17) is valid for  $G(\mu)$  as well as  $G$  constant. However, if  $G$  or  $\Gamma$  were to have an energy or temperature dependence, the P-V-E equation-of-state would not have had the form of Equation (A-14) which lead to Equation (A-17).

### 3. Computer Methods

As mentioned previously, the differential equations of motion governing the propagation of finite disturbances through a fluid are non-linear. Accordingly, the task of finding analytical solutions for a given set of initial and boundary conditions generally is extremely complicated, if not impossible. However, high speed computers provide the means for obtaining numerical approximations to the solutions.

At KSC the major computer program used in shock wave calculations is the PUFF V-EP hydrocode. Two kinds of initial conditions have been developed for the PUFF code: (a) an x-ray energy deposition calculation, and (b) a calculation corresponding to plate slap (i.e., the experimental situation where a projectile plate strikes a target

plate or plates). In order to conduct calculations from either initial situation, it is necessary to start with the equations-of-state of the materials of interest. Generally, experimental data provide only incomplete equations-of-state  $E(P,V)$  for the materials. The PUFF code then assumes the Mie-Grüneisen (P-V-E) equation-of-state to be valid so that a more complete thermodynamic description is available. The only requirement is, therefore, that the  $E(P,V)$  incomplete equations-of-state for the materials be expressed in a form compatible with the equation-of-state formulation used in PUFF, that is,

$$P = P_H(\mu) \left[ 1 - \frac{G\mu}{2} \right] + G\eta E \quad (A-18)$$

where

$$P_H(\mu) = C_H\mu + D_H\mu^2 + S_H\mu^3 \text{ (mb)}, \quad (A-19)$$

$$\eta = \rho/\rho_0 ,$$

and

$$E = \text{internal energy (mb)}.$$

This formulation is identical to Equation (A-17) except that  $\eta$  replaces  $\rho$  in the last term so that the internal energy is expressed in units of megabars and the initial energy is taken to be zero.

The form of the PUFF equation-of-state, Equation (A-18) is sometimes written in the equivalent form

$$P = C\mu + D\mu^2 + S\mu^3 + G\eta E \quad (A-20)$$

where the coefficients C, D and S are the "zero energy" coefficients. In order to determine these coefficients, the Hugoniot equation-of-state, Equation (A-19), is first defined by choosing the  $C_H$ ,  $D_H$  and  $S_H$  which best fit Equation (A-19) to experimental data. The zero energy coefficients are then obtained from the relationships:

$$C = C_H \quad (A-21a)$$

$$D = D_H - C_H \frac{G}{2} \quad (A-21b)$$

$$S = S_H - D_H \frac{G}{2} \quad (A-21c)$$

Laboratory experiments performed at KSC and reported herein were specifically designed to obtain data compatible with either Equation (A-18) or (A-20). Derivation of computer code inputs from raw experimental data is described in Part 4.

#### 4. Derivation of Computer Code Inputs

##### a. Determination of $P_H(\mu)$

Experimental techniques and equipment used at KSC for obtaining equation-of-state information are described in detail in Appendix B. The raw experimental data from Hugoniot tests such as described there are individual points on the test material's  $P_H - u$  Hugoniot curve. In order to obtain the  $P_H(\mu)$  Hugoniot required for PUFF calculations, the  $P_H - u$  data points may be converted to points in the  $P_H - \mu$  plane by using equations derived from the Hugoniot jump conditions, Equations (A-3). For given values of  $P_H$  and  $u$ ,  $U$  is first calculated using

$$U = \frac{P_H}{\rho_O u} \quad (A-22)$$



The Grüneisen parameter  $\Gamma(V)$  may be expressed in terms of other thermodynamic quantities by differentiating the Mie Grüneisen equation-of-state Equation (A-14) with respect to  $E$  at constant  $V$ . Then, since  $\Gamma$  is a function of volume only,

$$\Gamma(V) = V \left( \frac{\partial P}{\partial E} \right)_V . \quad (A-24)$$

Two approaches may be taken to estimate  $\Gamma$  using Equation (A-24). First, using basic thermodynamic identities, Equation (A-24) may be rewritten.

$$\Gamma(V) = V \frac{(\partial P / \partial T)_V}{(\partial E / \partial T)_V} \equiv \frac{V}{C_V} \left( \frac{\partial P}{\partial V} \right)_T \left( \frac{\partial V}{\partial T} \right)_P . \quad (A-25)$$

Equation (A-25) indicates that  $\Gamma$  may be evaluated from data for the isothermal bulk modulus, the volume coefficient of expansion and the specific heat. If  $\Gamma$  is assumed to have a constant value  $G$ , then

$$G = \frac{B\alpha}{\rho_0 C_V} \quad (A-26)$$

where

$$\begin{aligned} B &= \text{isothermal bulk modulus,} \\ \alpha &= \text{volume coefficient of expansion,} \\ \rho_0 &= 1/V_0 = \text{initial density,} \end{aligned}$$

and

$$C_V = \text{constant volume specific heat.}$$

The second approach for estimating  $\Gamma$  requires having hydrostatic pressure-specific volume curves for a material at two initial temperatures. The Grüneisen parameter may be

then  $\mu$  is calculated from

$$\mu = \frac{u}{U-u} \quad (\text{A-23})$$

using  $U$  found from Equation (A-22) and the given value of  $u$ .

It is worthwhile to consider the accuracy of these standard techniques when they are applied to a fairly compressive material. The calculation of  $U$  from Equation (A-22) is sensitive to uncertainties or variations in initial density  $\rho_0$ . As  $u \rightarrow U$ , large percentage inaccuracies may also occur in the term  $(U-u)$  of Equation (A-23) as the result of small errors in the value of either variable. Consequently, a set of  $P_H$ - $\mu$  points determined from a series of tests on a material having significant sample-to-sample variation in  $\rho_0$  may be expected to exhibit considerable scatter, especially in the region for which  $u \rightarrow U$ .

For materials such as metals, sample-to-sample variations in  $\rho_0$  are usually about 1% of the average value and, for shock levels encountered in gas gun testing,  $u$  is commonly less than 20% of  $U$ . In the case of porous materials, sample-to-sample variations in  $\rho_0$  are typically a few percent and  $u$  typically has values ranging up to a significant percentage of the calculated value of  $U$ . As expected, the  $P_H$ - $\mu$  points derived from the tests on porous materials exhibit significant scatter.

#### b. Determination of $G$

Once  $P_H(\mu)$  is determined, it is only necessary to have a value for the Grüneisen parameter  $G$  to complete the PUFF form of the equation-of-state.

determined from these hydrostats using Equation (A-24) written in the form

$$\frac{\Gamma(V)}{V} = \left( \frac{\Delta P}{\Delta E} \right)_V \quad (A-27)$$

The pressure change  $\Delta P$  at volume  $V$  is determined directly from the two P-V hydrostats. The difference in internal energy  $\Delta E$  between the materials at the two temperatures is made up of two parts. The first is the increase in thermal energy from heating the samples at constant pressure. It is found from

$$\int_{T_1}^{T_2} C_p dt \quad (A-28)$$

where  $C_p$  is the specific heat,  $T_1$  and  $T_2$  the two initial temperatures. The other term arises as a consequence of the different loading paths followed by the material at the two temperatures as it is compressed to the volume  $V$ . The total specific internal energy difference between the material at the two temperatures calculated as above, together with  $\Delta P$  from the hydrostats may then be used to estimate  $\Gamma(V)$ .

#### LIST OF REFERENCES

- A-1. R. Courant and K. E. Friedrichs, "Supersonic Flow and Shock Waves", (Interscience, New York, 1948).
- A-2 M. H. Rice, R. G. McQueen, and J. M. Walsh, in "Solid State Physics", Vol. 6 (1968).
- A-3 G. E. Duvall and G. R. Fowles, in "High Pressure Physics and Chemistry, R. S. Bradley, Ed. (Academic Press, Inc., New York, 1963), Vol. 2.
- A-4 G. D. Anderson, D. G. Doran, and A. L. Fahrenbruch, "Equation of State of Solids, Aluminum and Teflon", Air Force Weapons Laboratory Technical Report No. AFWL-TR-65-147 (1965).

## APPENDIX B

### EXPERIMENTAL TECHNIQUE

The purpose of this appendix is to describe the KSC gas gun facility and the experimental techniques used in conducting tests.

#### 1. Gas Gun Facility

The KSC gas gun facility includes one single-stage gun with a 24-foot length, 3-3/4-inch bore barrel and its associated equipment. The facility is shown schematically in Figure B-1. Compressed nitrogen or helium is used to propel flat-nosed aluminum projectiles against flat targets or curved nose projectiles against curved targets. All functions of the high pressure gas system are controlled and monitored remotely from a console outside of the bunker containing the gun itself. Projectiles weighing approximately 1 Kg may be propelled at impact velocities of from 0.01 to 0.09 cm/ $\mu$ s. Impact velocities less than 0.01 cm/ $\mu$ s may be achieved by utilizing projectiles weighing 2.0 - 3.0 Kg. A preselected impact velocity is usually achievable within about 5% over the range 0.02 - 0.09 cu/ $\mu$ s, with slower velocities preselectable to between 10% and 20%. A typical projectile is shown diagrammatically in Figure B-2.

In order to prevent air cushion effects from occurring during experiments, the barrel and target areas are evacuated prior to firing. Typical values for the barrel vacuum at impact time are between two and three microns, with the vacuum in no case being greater than 10 microns. Both sides of the target assembly are evacuated to prevent

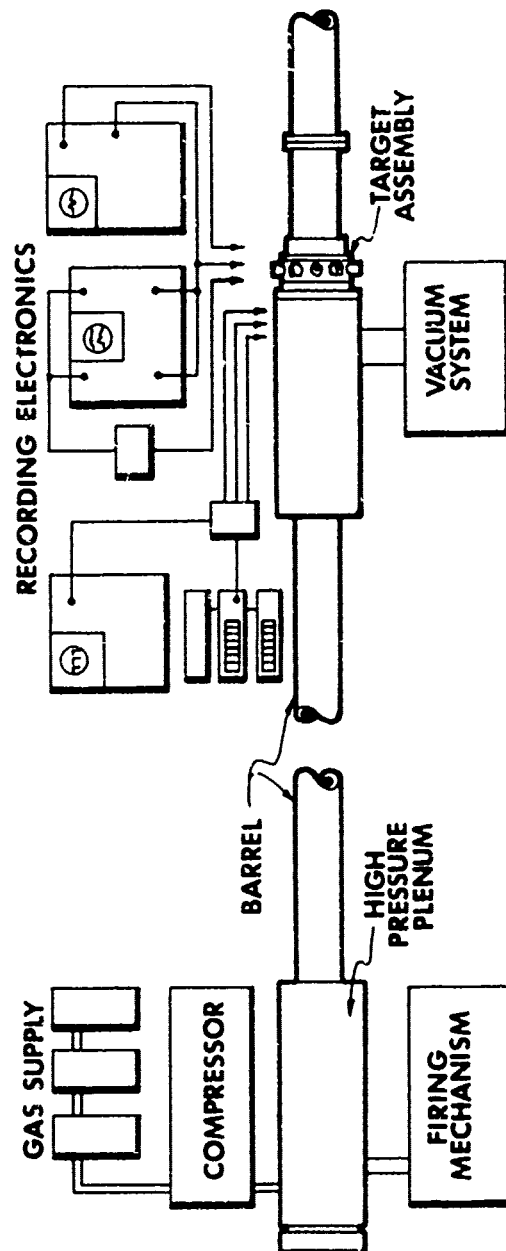


FIGURE B-1 SCHEMATIC DIAGRAM OF KSC GAS GUN FACILITY

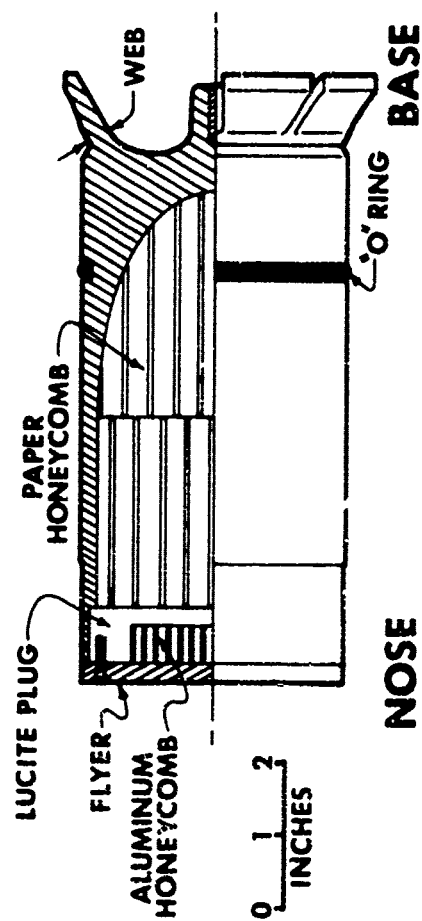


FIGURE B--2 TYPICAL GAS GUN PROJECTILE

pressure differences from causing target misalignment. All functions of the vacuum system are controlled and monitored remotely from the same console used in conjunction with the high pressure gas system.

The actual impact velocity achieved in an experiment is measured using a linear array of velocity pins located near the impact plane. This array of three shorting pins protrudes through the side of the gun barrel. Each pin is part of a discharge circuit which provides a sharp voltage spike when the pin is shorted to ground by the passage of the projectile. The intervals between the resulting voltage spikes are recorded in two ways. First, the spikes are displayed on an oscilloscope sweeping at a rate appropriate for recording all three spikes during a single sweep. Second, the spikes are used to start and stop a pair of high-speed timing counters. The first counter records the interval between the first and second pins while the second counter records the interval between the second and third pins. Accurate knowledge of the distances between pins then allows calculation of the impact velocity. Part of the uncertainty in velocity measurements using this system stems from inaccuracies in resetting the inter-pin distances during the setup for each shot. These distances are repeatable from shot to shot to about 0.2%. Additional uncertainty stems from the sensitivity of the recording circuitry to noise and jitter associated with the shorting of the pins. The overall accuracy of the system is estimated to be about 1%.

It is usually necessary to use additional contact pins either flush with the impact plane or a known distance in front of it, for the purpose of providing triggering or



timing signals for recording instruments or for measuring the amount of tilt during impact. Such pins are used in connection with specially designed electronic circuits to accomplish the desired task.

The stress history experienced by the impacting materials is obtained from the recorded output of one of several transducers. The use of each of these transducers is described below.

## 2. Set-Up and Alignment Procedures

In all gas gun experimentation, it is important to minimize the relative tilt between projectile and target. Since shock wave velocities are nearly always much larger than the associated particle velocities for shock strengths commonly attained with a gas gun, any relative tilt between the impacting surfaces will result in a great tilt of the shock front. The set-up procedures described below are designed to insure proper projectile-target alignment.

### a. Projectile Preparation

The projectile consists of a hollow cast aluminum cylinder, open at the front end and provided with a heavy base plate at the other, as shown in Figure B-2. A precision lip is machined at the open end so that materials may be mounted on the nose. The bulk of the cylinder is first filled with a paper honeycomb as a stiffening and strengthening material; then a lucite plug is fitted on the precision lip to provide a base for attaching the flyer. For direct impact shots in a flat geometry, an aluminum flyer is mounted on the lucite plug and the sample material glued in a shallow cup in

the flyer. The base of the bullet is lapped to insure it is perpendicular to the axis of the cylinder, then the nose is precision ground to make the nose flat and parallel to the base. The nose and the base are maintained parallel to better than 0.005 mm across the entire width of the bullet.

For transmitted wave shots in either flat or curved geometry, it is often desirable to have an unsupported rear surface on the flyer, e.g., for narrow pulse testing. In order to approximate this, open cell aluminum honeycomb is usually placed in a centrally located cup in the lucite plug prior to mounting the flyer. The honeycomb provides mechanical support against setback forces when the bullet is fired, but appears to have near zero shock impedance with respect to a shockwave propagated to the rear of the flyer. For tests in which the flyer is mechanically strong enough to withstand the setback forces, no supporting material is used. For thick flyer (long pulse) tests in either flat or curved geometry, the flyer is mounted directly on the lucite plug. The surface is lapped for the flat geometry or fly-cut on a milling machine for the curved geometry. The remainder of a bullet for transmitted wave shots is the same as described above for a direct impact shot.

#### b. Target Alignment

The alignment tool (slug) is a 46 cm long cylinder which closely fits the bore of the gun barrel. The slug has been precision machined and lapped to insure that its face is flat and perpendicular to the axis of the cylinder. The alignment procedure is begun by placing the slug in the gun barrel with its face a short distance from the plane of the face plate. Figure B-3 shows the alignment tool in use with

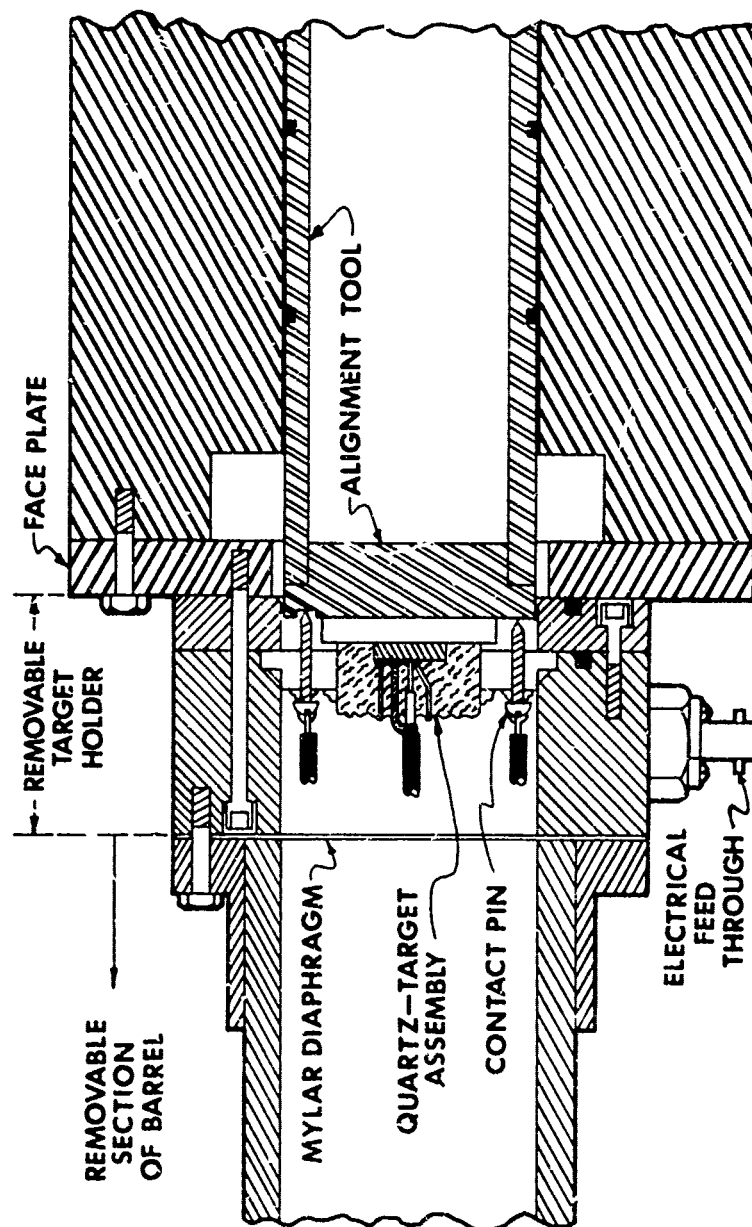


FIGURE B-3 TARGET ALIGNMENT

a quartz gage-target assembly. The target holder and electrical feed-through assembly is then bolted to the face plate. For a flat geometry test, the target-gage assembly is pressed firmly against the face of the slug and is bonded to the lucite holder with quick-set epoxy. Slight mechanical pressure is used to maintain the assembly in close contact with the slug while the epoxy bond is curing. Care is taken during this whole procedure to keep the faces of the target and slug very clean. For a curved geometry test, the target-gage assembly is precisely located in the lucite holder and is bonded in place before the lucite is mounted in the gun. The lucite fixture is provided with an indexing slot which mates with a precision key on the target holder, enabling correct positioning of the target-gage assembly to be achieved.

It is usually necessary to use contact pins, either flush with the impact plane or a known distance in front of it, for the purpose of providing triggering or timing signals for oscilloscopes or for measuring the amount of tilt during impact. The contact pins consist of fine threaded screws with coaxial cable attached. The screws are threaded through the lucite holder until contact is made with the face of the slug. For the purpose of aligning pins in front of the impact plane, the slug has several precision steps machined in its face. As the target-gage assembly is bonded in place, the screws are checked to assure that all make electrical contact with the slug face simultaneously, then they are also bonded in place with quick-set epoxy.

After the glue bonds have cured sufficiently, the coaxial cables are "plugged in" to the specially designed feed-throughs and electrical continuity is tested. The

signal leads from the gage are also checked for electrical continuity. After the mylar diaphragm is inserted and the removable section of the barrel replaced, the slug is extracted through the breech end of the gun barrel. Finally, the projectile is loaded and the breech end is closed.

### 3. Piezoelectric Quartz Gage

#### a. Basic Quartz Gage Relationships

The action of a quartz transducer is illustrated in Figure B-4. Assume a properly oriented crystal (Reference B-1) of thickness  $\ell$  and face area  $A$  is impacted on one face so that it experiences a uniform stress  $\sigma_\ell$  on that face. This stress propagates through the quartz as a shock wave with constant velocity  $U_g$  toward the backface which is under a uniform initial stress  $\sigma_0$ . The two faces are plated with a conductive material, such as gold, and are connected through a low resistance  $R$ . The voltage developed across this resistance is measured by an oscilloscope. If the polarization  $P$  is a function of the pressure  $\sigma_\ell$ , the electric displacement is

$$D = E + P(\sigma_\ell) \quad (B-1)$$

and the shock front in the quartz divides it into two regions, one polarized and one not polarized. The electric moment of a volume element  $d\tau$  is  $Pd\tau$  and, if electrical conductivity is negligible, the integral of this is equal to the product of the total charge  $Q$  on a face of the disc, and its thickness  $\ell$ . The increment of charge on a face in time  $dt$  is then

$$dQ = (A/\ell)dt \frac{\partial}{\partial t} \int_0^\ell P(\sigma_\ell) dx . \quad (B-2)$$

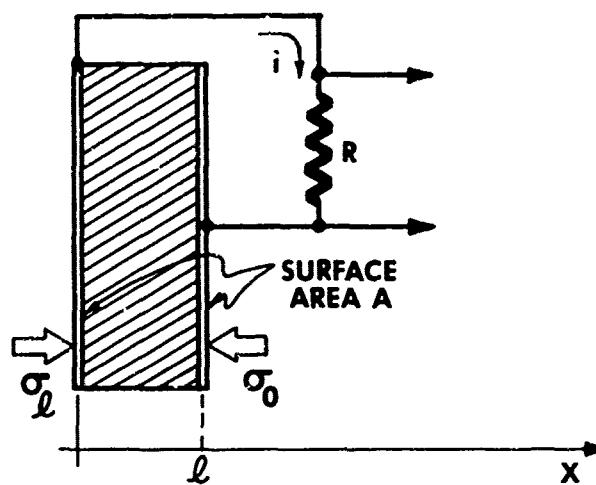


FIGURE B-4 ACTION OF QUARTZ TRANSDUCER

Since the faces of the disc are electrically connected,  
 $dQ/dt = i$  the external current flowing, and

$$i = (A/\ell) \int_0^{\ell} \frac{\partial P}{\partial t} dx \quad . \quad (B-3)$$

It is found experimentally for waves propagating in the +x direction that the polarization P is related to the stress  $\sigma_{\ell}$  over a wide range of pressures by a constant piezoelectric factor  $\epsilon$ ; i.e.,  $P = \epsilon \sigma_{\ell}$  for  $\sigma_{\ell} = \sigma_{\ell}(x-U_q t)$ . Then

$$\frac{\partial P}{\partial t} = \epsilon \frac{\partial}{\partial t} [\sigma_{\ell}(x-U_q t)] = -\epsilon U_q \sigma'_{\ell}(x-U_q t) \quad (B-4)$$

and

$$i = \frac{\epsilon A U_q}{\ell} [\sigma_o - \sigma_{\ell}] \quad . \quad (B-5)$$

Before the wavefront reaches the rear surface of the disc, the current is proportional to the pressure on the front face, and the gage is generally used only during this interval (References B-2, B-3).

#### b. Gage Construction and Calibration

Experiments at Kaman Sciences are performed using quartz crystals such as shown pictorially in Figure B-5. The small center electrode surrounded by a guard ring reduces edge effects and insures that Equation (B-5) accurately describes the effects observed. Typical electrical connections are indicated in Figure B-6. The voltage output history of the quartz gage upon passage of a shock wave is recorded photographically on a suitable oscilloscope. The data are later digitized and interpreted by the computer code FILMRD

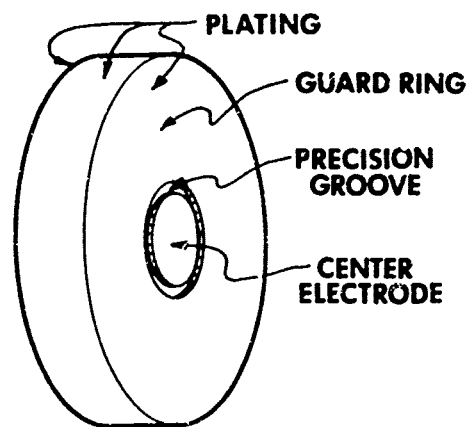


FIGURE B-5 QUARTZ CRYSTAL WITH SHORTED GUARD RING

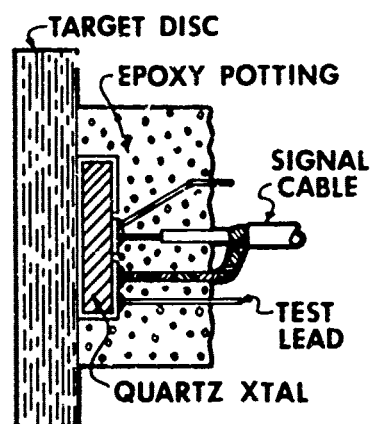


FIGURE B-6 TYPICAL QUARTZ-TARGET ASSEMBLY



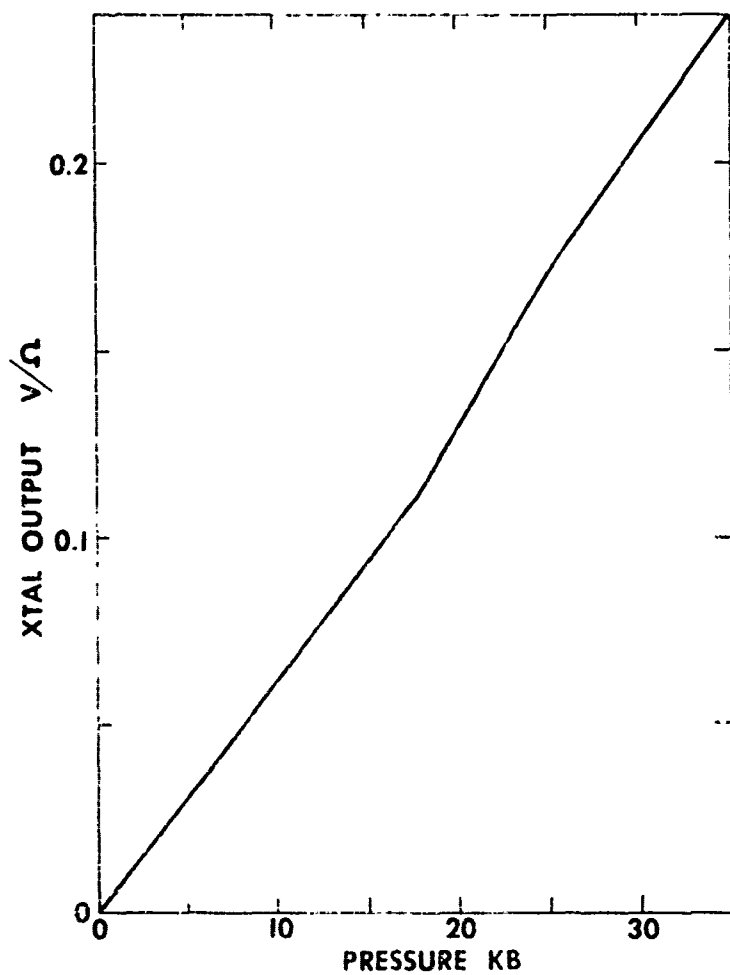


FIGURE B-7 CALIBRATION CURVE FOR 1" x 1/4" QUARTZ CRYSTAL

using the proper quartz calibration curve. Measurements of  $\epsilon$  enable a calibration curve such as Figure B-7 to be plotted for a particular crystal geometry so that only knowledge of the terminating resistance at the oscilloscope is required to transform the recorded voltage history into a pressure history. The final data is in the form of particle velocity or stress vs. time profiles.

For normal Hugoniot testing and certain types of transmitted wave testing, a 1-inch diameter, 1/4-inch thick, 1/4-inch diameter center electrode gage is used. When it is desirable to have a somewhat higher output from the gage for a given pressure history, a 2-inch diameter, 1/2-inch thick, 1/2-inch diameter center electrode gage is used. The output from this gage is approximately twice that of 1-inch x 1/4-inch gage under the same loading conditions. The 2-inch diameter by 1/2-inch thick gage is also used for many transmitted wave tests of materials when a longer recording time is required than is provided by the 1/4-inch thick gage.

In preparing a target assembly with a quartz crystal, the quartz is first bonded to the target disc(s) using a very thin layer of slow curing epoxy. The assembly is then measured and compared with the dimensions of the parts before gluing to insure a glue bond thinner than 0.002 mm. Signal and test leads are then soldered to the quartz crystal as shown in Figure B-6. Next, a mold is placed over the quartz crystal and leads and filled with epoxy potting compound. After curing, the mold is removed and the target quartz assembly is ready for mounting in the target holder. For a direct impact configuration, in which a bare faced quartz crystal is impacted directly by a sample mounted in

the projectile, the potting of the gage is performed on a precision flat plate coated with a type of mold release. After the epoxy has cured, the potted gage is removed from the plate and its front surface thoroughly cleaned.

#### d. Testing of Porous Materials

The relationships for quartz crystals mentioned above are based upon the assumption that the pressure  $\sigma_\ell$  is applied uniformly over the crystal face. If a quartz crystal is impacted by a highly porous material, the stress on the quartz may appear to be a large number of point loads rather than a uniform pressure. For slightly porous materials, this effect may only result in a very "noisy" piezoelectric output from the quartz. For some very porous materials, however, the non-uniform loading can make the quartz output undecipherable. One method of handling this situation experimentally is to interpose a material of high shock impedance, called a buffer, between the porous sample and the quartz.

The action of a buffer disc on the shock front produced by a porous material can be seen by reference to Figure B-8. If the average pore size is  $S$  and the points of contact are considered to be centers of origin of spherical wave fronts traveling with velocity  $U$ , then the shock front is smoothed out after traveling a distance of a few times  $S$  into the buffer. To insure that this takes place as quickly as possible, the buffer is usually fabricated from a material of very high shock impedance such as cemented tungsten carbide or Lucalox<sup>\*</sup>.

---

<sup>\*</sup> Registered Trademark, G. E. Lamp Division.

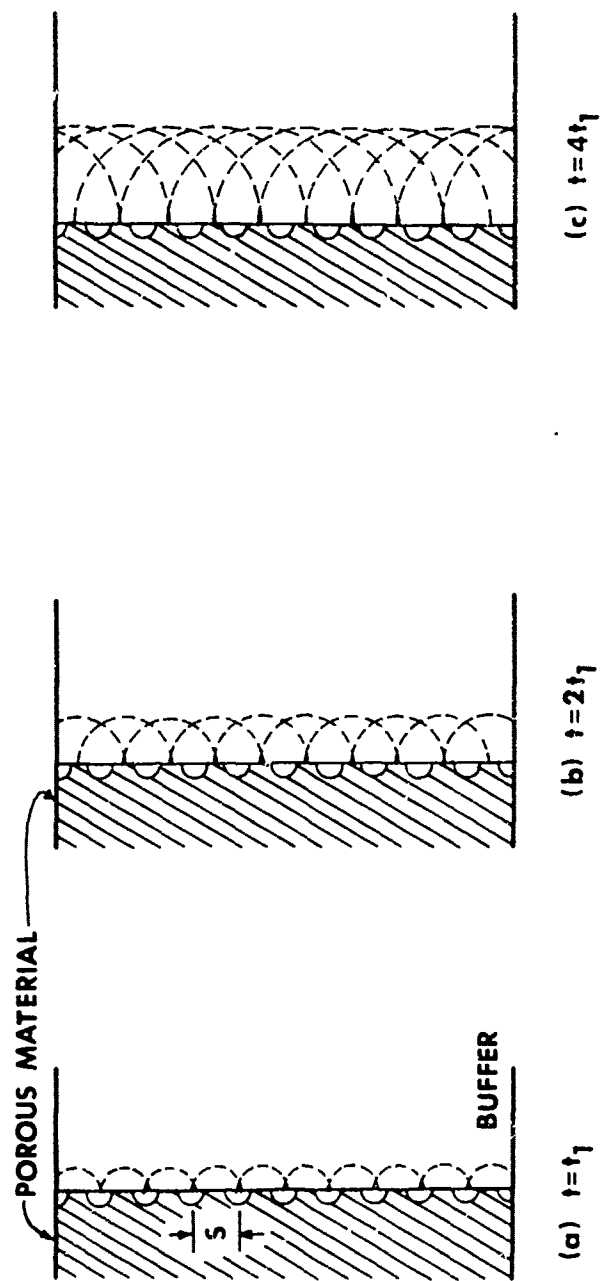


FIGURE B-8 ACTION OF BUFFER DISC ON SHOCK FRONT

A high shock impedance buffer also produces an additional desirable effect during Hugoniot testing of porous materials. Consider the impact of two materials. If the impact velocity is  $I$ , then to a first approximation the pressure generated by the impact  $P_O$  will be given by

$$P_O = \frac{1}{\left(\frac{1}{\rho_O c_O}\right)_{\text{MAT'L 1}} + \left(\frac{1}{\rho_O c_O}\right)_{\text{MAT'L 2}}} \quad (\text{B-6})$$

where  $c_O$  is the zero pressure sound speed and  $\rho_O$  the initial density of the materials. Suppose we have a disc of porous material of density  $1 \text{ gm/cm}^3$  and wave velocity  $0.2 \text{ cm/}\mu\text{sec}$  and wish to impact it on (a) a similar disc, (b) a quartz disc of density  $2.65 \text{ gm/cm}^3$  and wave velocity of  $0.57 \text{ cm/}\mu\text{sec}$  and (c) a tungsten carbide disc with density  $14.9 \text{ gm/cm}^3$  and wave velocity  $0.70 \text{ cm/}\mu\text{sec}$ . The pressure resulting from these three types of impacts will be

- a)  $P_O = 0.100(I)$       porous mat'l  $\rightarrow$  porous mat'l
- b)  $P_O = 0.177(I)$       porous mat'l  $\rightarrow$  quartz
- c)  $P_O = 0.196(I)$       porous mat'l  $\rightarrow$  WC

where  $P_O$  is in Mb for  $I$  in  $\text{cm/}\mu\text{sec}$ . Clearly, case c) generates roughly twice as much pressure at a given impact velocity as does case a). This affect is important when it is desired to test a material to as high a pressure as possible utilizing a gas gun with an upper limit to the impact velocity achievable. Recent porous material testing at KSC has been accomplished using tungsten carbide buffers for both direct impact and transmitted wave experiments. Tungsten carbide is linearly elastic under compressive loading to

nearly 100 Kb pressure and its properties are well known, hence interpretation of experimental records is simple when using the material as a buffer.

#### 4. Piezoresistive Manganin Gage

When it is necessary to observe a stress history during shock testing for a period longer than the useful quartz gage recording time (length of one shock wave transit), a piezoresistive manganin grid gage is usually the transducer chosen. Very long recording times ( $> 10 \mu\text{sec}$ ) have been obtained with the gages on the KSC gun, so they have been particularly useful for transmitted wave testing of materials which spread shock waves out in time.

The KSC gas gun facility uses a manganin grid gage of  $48.5 \Omega$  nominal zero pressure resistance (micromeasurements type VM-SS-210AW-0485). The gage consists of a 0.0005-inch thick photoetched manganin foil grid with integral lead configuration. The active element, which is 0.25-inch square, is made up of 28 legs connected to two copper-plated, 0.1-inch wide foil leads. The gages come from the manufacturer mounted on 0.001-inch Kapton tape.

##### a. Basic Manganin Gage Relationships

In use, the manganin gage is connected so that it forms one arm of a Wheatstone bridge circuit. When the gage is compressed, its resistance increases, causing the bridge circuit to become unbalanced. Since the unbalanced condition causes a voltage to be developed across the null indicator of the bridge, the voltage history occurring across the null indicator can be recorded and used to obtain a stress history.

The relative change in resistance is small for pressure changes normally encountered in laboratory testing, so that a driving voltage of several hundred volts must be used across the bridge in order to obtain a signal of convenient size. For this reason, the gage is required to dissipate considerable power. To avoid destroying the gage, the power supply is designed so that it may be triggered on shortly before the pressure wave is expected at the gage. In addition, a "crow-bar" circuit is provided for the bridge which shorts out the gage arm after a preset time. This last feature allows pre-shot testing to be done using a very short duration for the power pulse applied to the gage. The power supplies used at KSC are all Luchter "Piezoresistive Gage Pulse Power Supply" units.

It is found experimentally that the relative change in resistance of the manganin gage is a second-order function of pressure, e.g.,

$$\frac{\Delta R}{R} = \alpha P + \beta P^2, \quad (B-7)$$

where  $\alpha$  and  $\beta$  are parameters determined experimentally for each different gage configuration. The voltage history of the null indicator of the bridge is displayed on an oscilloscope and recorded photographically during a test. The resulting record is later digitized and reduced by a computer program (MANGDAT) to stress vs. time profiles.

#### b. Gage Fabrication

The grids are made up into transducers in two ways. For certain materials, a gage is potted directly on the back of a sample for transmitted wave testing. With conductive

samples, the gage is insulated from the sample by 0.001-inch Kapton tape.

The preferred geometry for the transducer, however, has the grid mounted between two pieces of 6061-T6 aluminum. This gage "sandwich" consists of ~0.060" aluminum face plate, the manganin grid between two pieces of 0.001-inch Kapton tape and a thick back block of aluminum. The assembly is bonded together with Epon 815 epoxy and can be used either for transmitted wave tests, by bonding it to the rear face of a sample, or for direct impact tests. The manganin-in-aluminum gage can be fabricated in either a flat or curved geometry (see Section 5 below). For the flat gage, the aluminum face plate and back block are machined to a cylindrical shape and the plane surfaces are lapped to insure flatness. For the curved gage, the face plate and back block are arc segments cut from appropriately sized rings. In either gage assembly, the leads are protected from shock and handling by a rubber sealing compound (G.E. RTV 108) at the point where they exit from between the aluminum blocks.

The thin face plate in front of the grid acts as a buffer plate which smooths out the shock front from non-homogeneous materials so the grid is not adversely affected by uneven shock loading.

## 5. Curved Sample Testing

For certain types of materials; e.g., fiber reinforced composite materials, testing of samples in the shape of flat faced discs is of limited utility, due principally to the cylindrical or conical geometry used in the fabrication of the materials. To overcome this limitation in gas gun testing,



KSC has developed the technique of using cylindrically shaped flyers mounted on non-rotating projectiles and impacting targets in the form of arcs cut from material originally fabricated in cylindrical geometry. Prior to the launch of the projectile, both the projectile and target are accurately aligned using an indexing device referenced to absolute horizontal. The degree of asynchronicity during impacts in the curved geometry has been tested and found to be acceptable considering the dimensional tolerances associated with materials which would logically be tested in this manner. The most useful transducer for this type of testing is the manganin gage, fabricated in cylindrical rather than flat form. Problems do not arise in using a gage such as this as long as the effective diameter of the curved surface containing the gage is not too small. Successful tests have been performed using effective diameters of from ~12 cm to 25 cm.

#### 6. Additional Gas Gun Techniques

In addition to the quartz and manganin transducers described above, the KSC gas gun facility also uses fully electroded quartz, a laser interferometer and magnetic particle velocity gages for certain types of experiments. Materials may also be tested using a two-quartz gage technique, shock reverberation techniques, or at elevated temperatures. These additional transducers and techniques have not been employed in testing reported here, hence are not described.

#### LIST OF REFERENCES

- B-1 R. A. Graham, "Dielectric Anomaly in Quartz for High Transient Stress and Field", Journal of Applied Physics, 33, 1755-1758 (1962).
- B-2 G. E. Duvall and G. R. Fowles, in "High Pressure Physics and Chemistry", R. S. Bradley, Ed. (Academic Press, Inc., New York, 1963), Vol. 2.
- B-3 R. A. Graham, F. W. Neilson, and W. B. Benedick, "Piezoelectric Current from Shock-loaded Quartz - A Sub-microsecond Stress Gauge", J. Appl. 36, 1755-1783 (1965).